Multi-Phase Fracture-Matrix Interactions Under Stress Changes

Sixth Semi-Annual Report

Reporting Period
March 21, 2004 – September 20, 2004

Principal Authors:
A.S. Grader, D. Elsworth, P.M. Halleck, F. Alvarado, A. Alajmi, Z. Karpyn,
N. Mohammed, S. Al-Enezi

Report Issue Date: June 15, 2005

DOE Award Number: DE-FC26-01BC15355

Submitting Organization:
The Pennsylvania State University
The Energy Institute
A.S. Grader
203 Hosler Building
University Park, PA 16802

DISCLAIMER

ABSTRACT

The main objectives of this project are to quantify the changes in fracture porosity and multi-phase transport properties as a function of confining stress. These changes will be integrated into conceptual and numerical models that will improve our ability to predict and optimize fluid transport in fractured system. This report details our progress on: **a**. *developing the direct experimental measurements of fracture aperture and topology and fluid occupancy using high-resolution x-ray micro-tomography,* **b**. *qunatifying the effect of confining stress on the distribution of fracture aperture* , *and* **c**. *characterization of shear fractures and their impact on multi-phase flow*.

The three-dimensional surface that describes the large-scale structure of the fracture in the porous medium can be determined using x-ray micro-tomography with significant accuracy. Several fractures have been scanned and the fracture aperture maps have been extracted. The success of the mapping of fracture aperture was followed by measuring the occupancy of the fracture by two immiscible phases, water and decane, and water and kerosene.

The distribution of fracture aperture depends on the effective confining stress on the nature of the rock and the type and distribution of the asperities that keep the fracture open. Fracture apertures at different confining stresses were obtained by micro-tomography covering a range of about two thousand psig. Initial analysis of the data shows a significant aperture closure with increase in effective confining stress. Visual descriptions of the process are shown in the report while detailed analysis of the behavior of the distribution of fracture aperture is in progress. Both extensional and shear fractures are being considered.

The initial multi-phase flow tests were done in extensional fractures. Several rock samples with induced shear fracture are being studies, and some of the new results are presented in this report. These samples are being scanned in order to quantify the distribution of apertures and the nature of the asperities. Low resolution images of fluids in a sample with a shear fracture were performed and they provide the confidence that flow patterns and saturations could be determined in the future.

A series of water imbibition tests were conducted in which water was injected into a fracture and its migration into the matrix was monitored with CT and DR x-ray techniques. The objective is to understand the impact of the fracture, its topology and occupancy on the nature of mass transfer between the matrix and the fracture. Counter-current imbibition next to the fracture was observed and quantified, including the influence of formation layering.

TABLE OF CONTENTS

LIST OF FIGURES

LIST OF TABLES

INTRODUCTION

Natural and artificially-induced fractures in a reservoir have a great impact on fluid flow patterns and on the ability to recover hydrocarbons. In tight formations, the naturally fractured system provides access to the hydrocarbon fluids stored in the matrix. Fractures can have a negative effect on recovery processes when they form bypassing paths, especially in production-injection systems. For example, injected fluid may preferentially flow through the fractures leaving behind inaccessible and non-contacted hydrocarbons. Fractures can enhance the efficiency of displacement operations when the main direction of flow is perpendicular to the direction of the fractures. Fractures may also be non-conductive and form barriers to fluid flow. The mass transport between the fractures and the surrounding matrix has an important role in being able to predict and optimize the recovery processes from fractured reservoirs. As production occurs and pore pressures decline, the net confining stress on the rock increases. This project focuses on the effects that changes in confining stress have on the transport properties of the fracture-matrix system. The confining stress has an impact on the fracture aperture and therefore on multiphase fluid transport properties (*Barton et al.*, 1985, *Gentier et al.*, 1997). We propose to quantify the changes in fracture porosity and saturation distribution under steady and non-steady flow in both the fracture and the adjoining matrix. The quantitative changes will be obtained by low and high resolution X-ray computerized tomography (CT) imaging (*Vinegar and Wellington*, 1987), and then these changes will be used in an inverse simulation process to quantify changes in permeabilities and to suggest up-scaling procedures.

We propose a fracture-matrix interaction program with the following objectives:

• Quantify the effects of confining stress on fracture topology and aperture and porosity.

• Quantify the changes in two-phase fracture permeabilities as a function of stress.

• Determine the effect of stress on oil-water transport between the fracture and the matrix.

• Determine the effects of stress on recovery processes in the presence of fractures.

• Use inverse simulation of four-dimensional saturation data for up-scaling.

We approach multi-phase flow in stressed fractured rocks experimentally and computationally. We will use multi-phase injection into confined rock samples that contain natural fractures or artificially induced ones. We will quantify the saturation distribution temporally and spatially (four-dimensional) using our new imaging facility and The Center for Quantitative Imaging. We will also monitor the pressure behavior of the sample and confining fluids. The resulting four-dimensional distribution of saturations and pressure histories will form the basis for multi-phase fluid flow simulation with the ultimate goal of quantifying the changes in the fluid flow characteristics of the rock as a function of the net confining stress. This combined experimental/computational approach will lead to advances in our understanding of the effects in-situ stress on recovery processes.

EXECUTIVE SUMMARY

The main objectives of this project are to quantify the changes in fracture porosity and multi-phase transport properties as a function of confining stress. These changes will be integrated into conceptual and numerical models that will improve our ability to predict and optimize fluid transport in fractured system. The project has five tasks:
1. Quantify the effects of confining stress on fracture topology and aperture and porosity.
2. Quantify the changes in two-phase fracture permeabilities as a function of stress.
3. Determine effects of stress on oil-water transport between the fracture and the matrix.
4. Determine the effects of stress on recovery processes in the presence of fractures.
5. Use inverse simulation of four-dimensional saturation data for up-scaling.
This report focuses mainly on tasks 1, 2 and 5.

Fracture Topology, Aperture, and Fluids: A new multi-phase experiment was conducted during the current reporting period. The experiment included the mapping of the distribution of fracture apertures and the distribution of two fluid phases in the fracture. There is a clear relationship between the presence of the non-wetting phase and the large fracture apertures, as expected from capillary stability considerations. The experiments included imaging while flowing and during segregation. The experiment was done at low confining stress using the newly designed and manufactured core holder. Significant effort has been devoted to managing and mining the three-dimensional digital data describing the experiment that included eight temporal sequences of more than three thousand micro-tomography slices per sequence.

Fracture Closure Under Confining Stress: The experiment documented in this report explored the ability of micro-tomography to quantify the changes in the distribution of fracture apertures with different confining stresses. The experiment was performed under dry conditions with an extensional fracture, and a confining pressure range between 100 and 2500 psig. The closure of the fracture is documented and we are in the process of quantifying the increase in the contact area, the decrease in fracture volume, and change in the distribution of fracture apertures.

Shear Fracture: Shear fractures have different properties than extensional fractures. We have artificially fractured several samples in shear mode and are currently studying the single- and two-phase fluid flow in these samples using external measurements of fluid volumes, pressure gradients, and internal saturation and structure measurements using micro-tomography. The absolute permeability of three samples was reduced by about 30% after the fracturing process. One sample (so far) was scanned to reveal a very complicated fracture and sub-fractures along the curved fracture surface. There are large asperities that are very different in structure than the asperities created in an extensional fracture.

Modeling of Fracture-Matrix Fluid Flow Interactions: Some previously performed two-phase flow experiments are being analyzed. In one of these experiments, a layered sample was fractured at the inlet end, with an axial fracture that extended only to the middle of the sample, creating a fracture tip. The oil loading process is being modeled. Two dimensional simulations are being integrated into a full three-dimensional model. Properties from the two-dimensional systems are used as the starting point for the three-dimensional simulations. Early results indicate that there is cross flow between the layers during the oil loading period.

EXPERIMENTAL METHOD AND PROCEDURES

The experimental system used in this project includes a multi-phase fluid flow system, a core holder assembly that can provide controlled confining pressure, and an x-ray computed tomography system. A schematic of the system is shown in **Figure 1** and photographs of the medical and the industrial scanners are shown in our first quarterly report. Most of the details of the fluid flow system can be found in *Alajmi and Grader* (2000). Two new core holders were acquired. These are tri-axial cells with high pressure ratings and elevated temperatures. The rock samples may have a diameter of up to 25 mm and a length of up to 300 mm. These core holders will be used to study the effects of confining stress and fracture aperture on two phase flow. A new core holder was designed and built for low confining pressure. This core holder is made of polycarbonate and is clear. The advantage of this low pressure core holder is that it has a low x-ray attenuation allowing efficient micro-tomography operations..

The Computed Tomography (CT) system consists of an ionized x-ray source, a detector, a translation system, and a computer system that controls motions and data acquisition. The x-ray source has a Tungsten target with a focal spot of 5 microns. It produces a cone beam that passes through the core and activates the detector. The image intensifier detector surface releases electrons that are then focused on a screen that is photographed by a high-resolution (1024x1024) camera with a frequency of 15 Hz. The sample is rotated 360 degrees in the x-ray beam while the detector is providing attenuation views to the data acquisition computer. After the sample is rotated a complete turn, the system reconstructs a slice, a cross-sectional image of the attenuation values that represents a combination of the density and the apparent atomic number of the sample and the imaged position. The imager operates in volume mode where

several separate slices are collected in one rotation. In the example shown in the report, up to 41 slices were acquired in a single rotation. After each rotation, the sample is translated axially to a new scanning position, thus, allowing a continuous three-dimensional coverage of the sample.

RESULTS AND DISCUSSION

MATRIX-FRACTURE INTERACTION – COUNTER-CURRENT IMBIBITION

This experiment focuses on mass transport between the fracture and the matrix under imbibition conditions. The entire core was oil saturated and then a fixed amount of water was injected strictly into the fracture and then allowed to equilibrate. Counter-current imbibition created water flow from the fracture to the matrix and oil flow from the matrix to the fracture. This is an essential process to understand and quantify as it is the main displacement production mechanism that allows us to extract hydrocarbons from matrix blocks into the transmitting fractured network.

Experimental System

An experimental two-phase model was designed to study fluid flow in fractured porous media. Visualization and quantification of fluid phases inside the fracture were acquired using X-ray computed tomography. A complete description of the equipment, materials, and procedures used is presented in this chapter.

Fluids and Rock Samples: The fluids used in the present experiments are distilled water, silicone oil, and decane. The physical properties of these fluids are shown in **Table 1** In order to determine the saturation of one phase using one X-ray energy level, it is necessary to transform the three-fluid system into a two-fluid system distinguishable by X-ray (Vinegar and Wellington, 1987). Highest resolutions in Micro-Computed Tomography are achieved with the help of a

tagging agent, which increases the X-ray attenuation of fluids. For the current flow experiments, silicone oil was mixed with 30% by weight of n-decane to form the oil phase, bringing its viscosity down from 20 cp to 5.0 cp. Water was tagged with 15% by weight of sodium iodide (NaI) in order to increase its CT registration, thus incrementing the contrast between the oil and water phases. The viscosity of tagged water increased to approximately 1.2 cp. The doping brings water to a high CT registration while oil has a lower CT registration.

Table 1: Physical Properties of Fluids

Name	*Viscosity at 25C (cp)*	*Density at 25C (g/cc)*	*Physical form*
Water, H_2O	0.890	0.9970	Liquid
Silicone oil, polydimethylsiloxane	20.0	0.9540	Liquid
n-Decane, $CH_3(CH_2)_8CH_3$	0.838	0.7300	Liquid

After treatment with tagging compounds, the oil and water phase were thoroughly mixed with each other and then were allowed to separate under gravity. Pre-saturation avoids inter-phase mass transfer during experiments and preserves mass balance. In all remaining experimental descriptions, "water phase" refers to distilled water tagged with sodium iodide, and the "oil phase" refers to silicone oil mixed with decane.

More than ten core samples were used throughout this experimental research including fracturing, preliminary test, dry scans, etc. However, only two of these samples were used in flow experiments 1 and 2, namely sample 1 and 2, respectively. Samples used were in its majority layered Berea sandstones (protoquartzite). Berea is a calcite-cemented sandstone with 5 % clay content, porosity ranging between 15-22 %, and unconfined compressive stress ranging from 6 to 15 ksi (Grader et al., 2000). The samples used in the experiment have a diameter of 25

mm, and a length of 47-100 mm. They were cored parallel to bedding and fractured with a modified Brazilian test.

The experimental installation used in this work includes a core holder assembly that can provide controlled confining pressure, a multi-phase fluid flow system, and a high- resolution X-ray Computed Tomography system.

Low-Pressure Core Holder: A new low-pressure core holder was designed and built for studying the distribution of fluids in the fracture under constant confining pressure. Figure 1 shows a diagram of the new core holder design. The polycarbonate core holder sleeve can accommodate a 25 mm diameter sample with up to 228.6 mm in length. Shorter samples require additional spacers also included in the design. Each of the two end-plugs has four ports: two fluid ports and two pressure ports. A diagram of the face of the end-plugs is shown in Figure 2. Detailed design diagrams and dimensions are provided in Appendix A. The face of the end-plugs was specifically designed to allow simultaneous injection of two phases in a fracture.

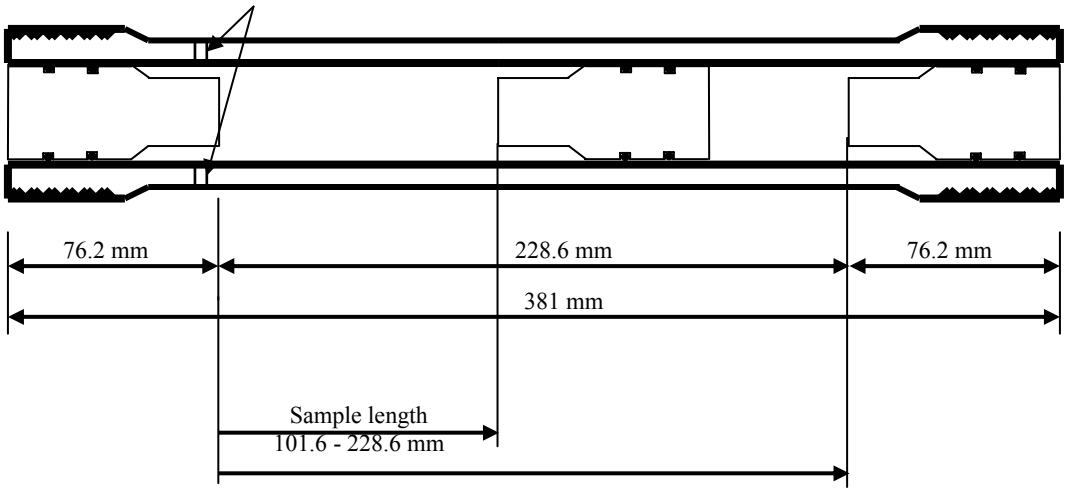

Figure 1: Overall view of the core holder sleeve.

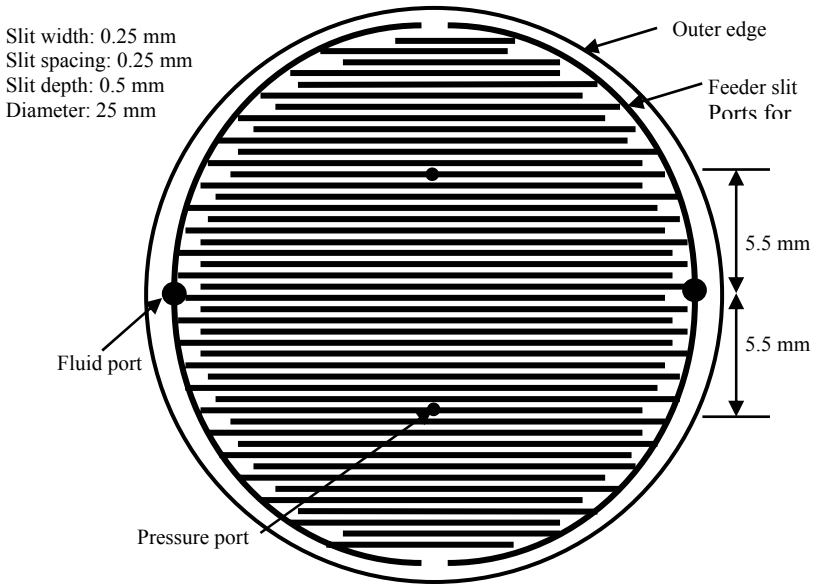

Figure 2: Top view of end-plug design.

The semi-circular channels at both sides of the end-plugs are the entry ports for the two fluids. These channels can also be seen in Figure 3 (right). From these two semi-circles, 0.25 mm channels traverse the face of the end-plug creating an alternating pattern for distributing the fluids into the face of the rock sample and the fracture. Figure 4 shows a photograph of all the pieces forming the new core holder.

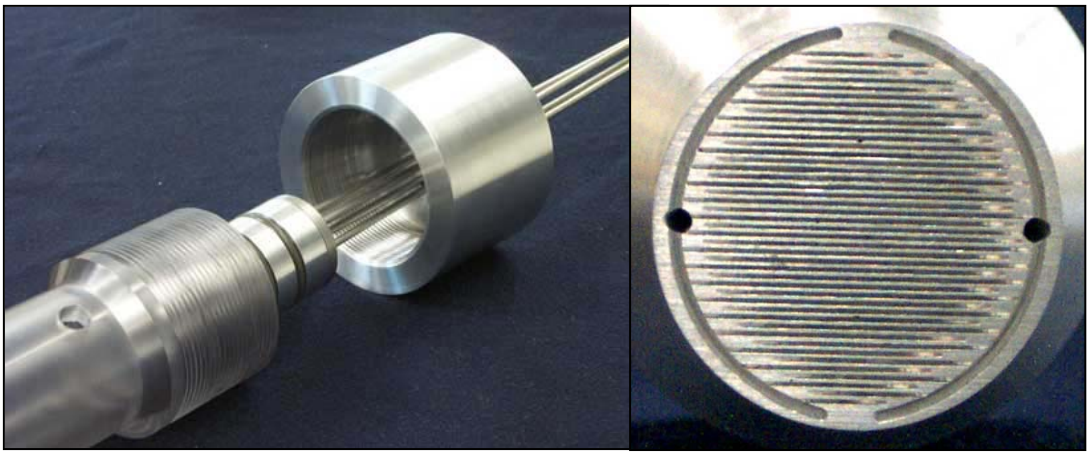

Figure 3: Core holder assembly (left) and end plug face (right).

Figure 4: Polycarbonate and aluminum core holder.

Fluid Flow System: A schematic of the fluid flow system is shown in Figure 5. This multi-phase fluid flow system can provide simultaneous injection of oil and water into the core. Oil and water are injected into the fractured sample in the upward direction. Pressure drop through the sample can also be recorded during fluid injection. Fluids leaving the sample are filtered and collected for re-injection.

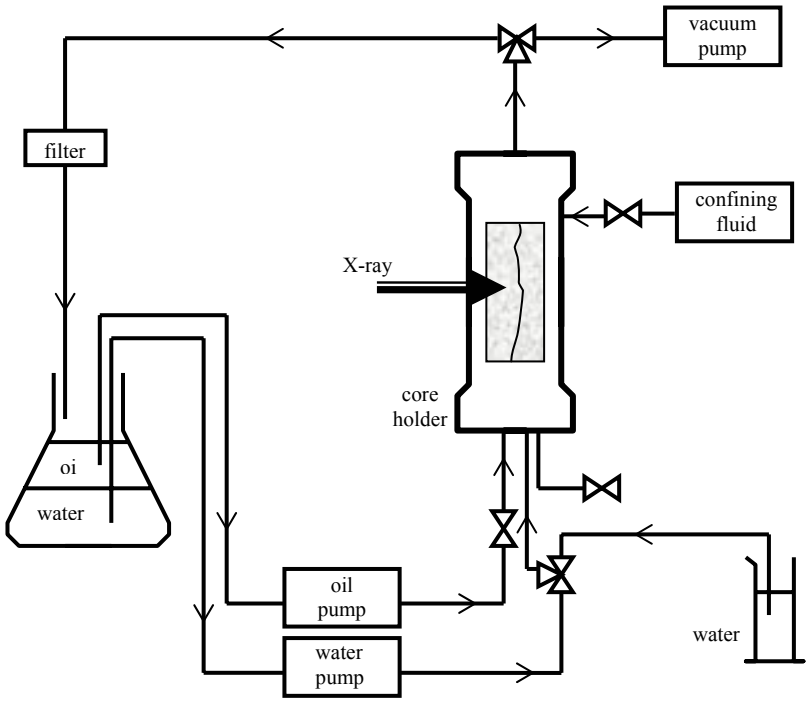

Figure 5: Schematic of experimental installation.

High-Resolution CT Scanner: X-Ray Computed Tomography (CT) is the technique used in this study to visualize and quantify fluid distribution as well as the inner structure of a rock fracture. Computed tomography is defined as a non-destructive imaging technique that uses X-rays and mathematical reconstruction algorithms to view a cross-sectional slice of an object

(Vinegar and Wellington, 1987). The image reconstruction is based on multiple X-ray measurements made through the object along different paths.

In the present work, several artificially created fractures are studied through visualization and quantification using Computer Tomography (CT). This state-of-the-art technology allows spatial pixel resolution ranging between 20 and 50 microns. At this resolution, hundreds and even thousands of two-dimensional slices form the three-dimensional digital core.

The Computed Tomography (CT) system consists of an ionized X-ray source, a detector, a translation system, and a computer system that controls motions and data acquisition. The X-ray source has a Tungsten target with a focal spot of 5 microns. It produces a cone beam that passes through the core and activates the detector. The image intensifier detector surface releases electrons that are then focused on a screen that is photographed by a high-resolution (1024 x 1024) camera with a frequency of 15 Hz.

The sample is rotated 360 degrees in the X-ray beam while the detector is providing attenuation views to the data acquisition computer. After the sample is rotated a complete turn, the system reconstructs a slice, a cross-sectional image of the attenuation values that represents a combination of the density and the apparent atomic number of the sample and the imaged position. The imager operates in volume mode where several separate slices are collected in one rotation. In this experimental study, up to 41 slices were acquired in a single rotation. After each rotation, the sample is translated axially to a new scanning position, thus, allowing a

continuous three-dimensional coverage of the sample. Figure 6 shows the core assembly mounted in the high-resolution CT scanner.

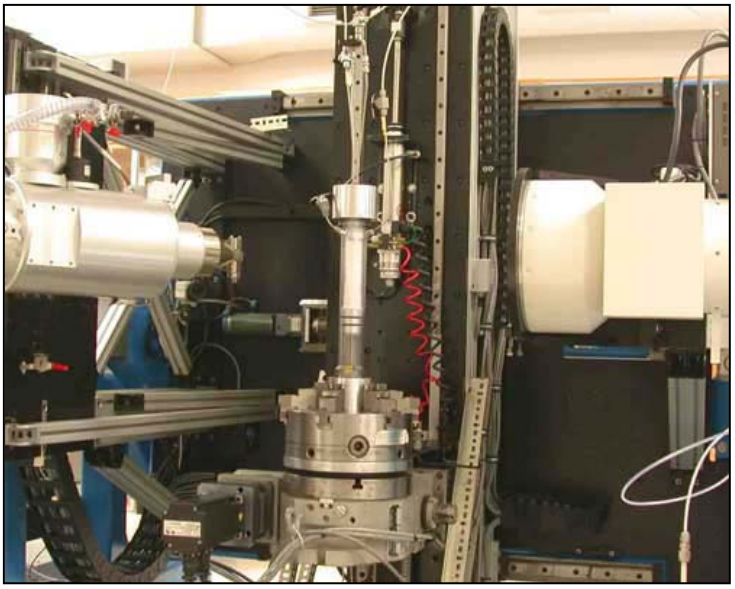

Figure 6: Core sample installed in high-resolution CT scanner.

Fracturing Apparatus: The apparatus used to fracture Berea samples was originally designed to create shear fractures, but its controlled load mechanism allows for tensile fracturing as well. A photograph of this apparatus is shown in Figure 7. The machine stiffness for the vertical load frame is 5 MN/cm. The vertical ram was controlled in load feedback. The position and exerted force of the ram are measured by displacement transducers and load cells mounted on the rams. Figure 8 shows the data collected for one of the Berea samples. On the initial portion of the curve, from left to right, normal stress is gradually increased up to the point of failure. At failure, there is a sharp decrease in recorded stress. The near-horizontal portion of the curve corresponds to the period of time in which the sample was being observed to verify the fracture had propagated properly. The last portion of the graph describes the off-loading of the sample.

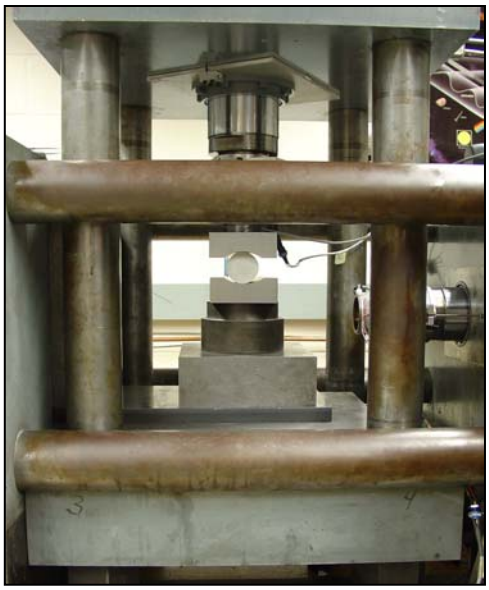

Figure 7: Servo-controlled biaxial loading apparatus used for tensile fracturing.

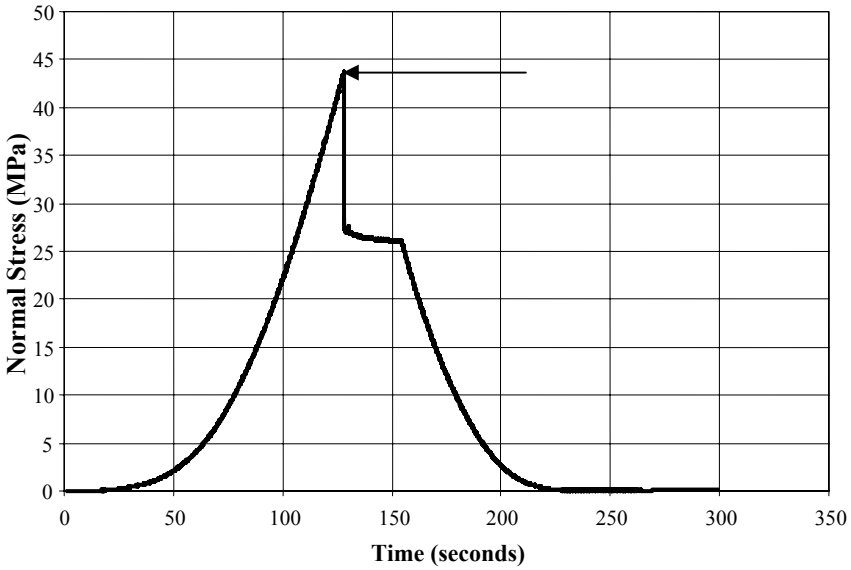

Figure 8: Normal stress versus time during the fracturing process.

Capillary Imbibition: The rock sample used in this experiment (Sample 2) was cored parallel to bedding and fractured perpendicular to bedding. Once the rock sample is fractured and separated into two halves, the two portions of rock are put back together with a slight shift of 0.4 mm along the longitudinal axis. This shift accentuates aperture changes inside the fracture. 0.4-thick plates were placed at the bottom of the core to maintain a flat contact with flow distributors. The pixel resolution used in this experiment was 0.030 mm x 0.030 mm and the slice thickness was 0.032 mm. Detail procedure of experiment 2 is described next. A schematic representation of the scanning sequence is shown in Figure 9.

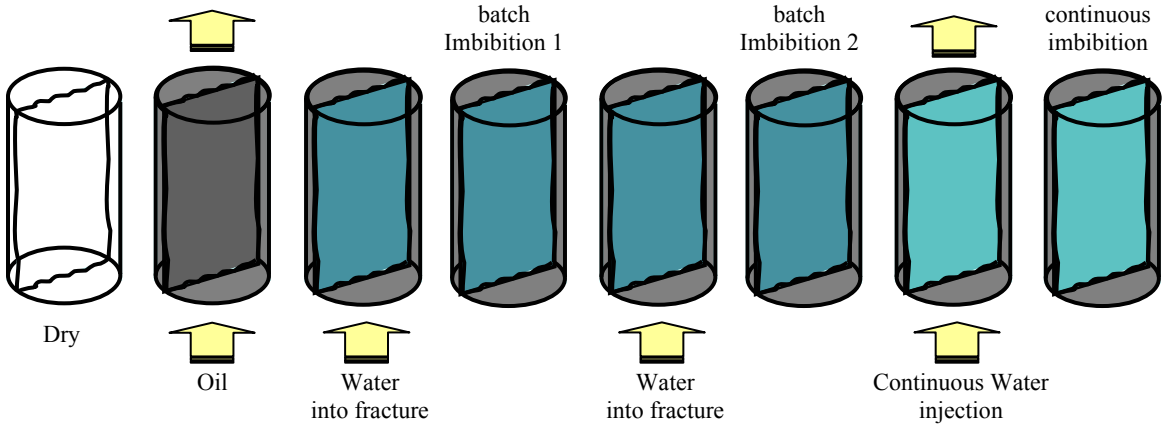

Figure 9: Scanning sequence of experiment 2: capillary imbibition.

1. Drill 50 mm-diameter Berea sample parallel to bedding plane.

2. Fracture Berea sample perpendicular to the rock bedding using modified Brazilian method.

3. Re-drill fractured sample to 25 mm in diameter.

4. Shift fracture faces by 0.4 mm.

5. Wrap sample with Teflon® tape and heat shrink tubing extended to end plugs. Seal heat shrink tubing against aluminum end-plugs and flow distributors.

6. Assemble rest of core holder pieces with sample inside. Tighten sample inside core holder using spacer rings.

7. Prepare fluids. There are two different fluid phases, oil and water. The oil phase is a mixture of 70 % silicone oil, and 30 % decane (viscosity reducer). Water phase contains distilled water and 15 % weight of NaI (tagging component).

8. Saturate fluids with each other and apply vacuum to remove dissolved air.

9. Measure fluid properties of prepared mixtures (oil and water).

10. Assemble experimental installation (tubing, valves, pumps, reservoirs, collectors, pressure gauges). Allow core holder and adjacent connections to rotate 360□ with the scanner table.

11. Displace air bubbles from flow lines.

12. Apply vacuum to core sample holding oil out. Let vacuum reach approximately 150 microns of pressure.

13. Inject confining fluid to fill the annulus between the sample and the walls of the core holder and stabilize confining pressure to 30 psig.

14. Calibrate scanner. The scanner operated at 160 kV and 200 □A, with a pixel resolution of 28.3 microns in x and y directions, and 32.2 microns in the z direction. Each slice is constructed using two 2400-views.

15. Scan 50 mm along the dry sample. This is done in 31 rotations, collecting 51 slices per rotation for a total of 1632 slices to cover approximately 50 mm. The entire scanning routine takes about five hours.

16. Vacuum saturate the sample with the oil phase. Measure volume consumed during oil saturation.

17. Select a region along the main axis on the sample to be the focal point during spontaneous capillary imbibition. Scan focal point for initial condition.

18. Inject approximately 1PV of tagged water into the fracture to displace resident oil. Water injection is upwards. This stage corresponds to batch imbibition 1. For fractures whose surfaces have been shifted, the fracture pore volume ranges between 2-3 % of the total cylindrical sample volume.

19. Start sequence of continuous scanning during spontaneous capillary imbibition.

20. Once spontaneous capillary imbibition has ceased, scan entire sample.

21. Repeat injection of tagged water into the fracture to displace resident oil, using 1.5 cc of water, and repeat steps 19 through 20. Water injection is upwards. This stage corresponds to batch imbibition 2.

22. Proceed with continuous injection of tagged water and repeat steps 19 through 20. Water injection is upwards.

Data collected during spontaneous imbibition include high-resolution scans at a fixed location and large-range digital radiographs. Fluid exchange takes place as represented in Figure 10.

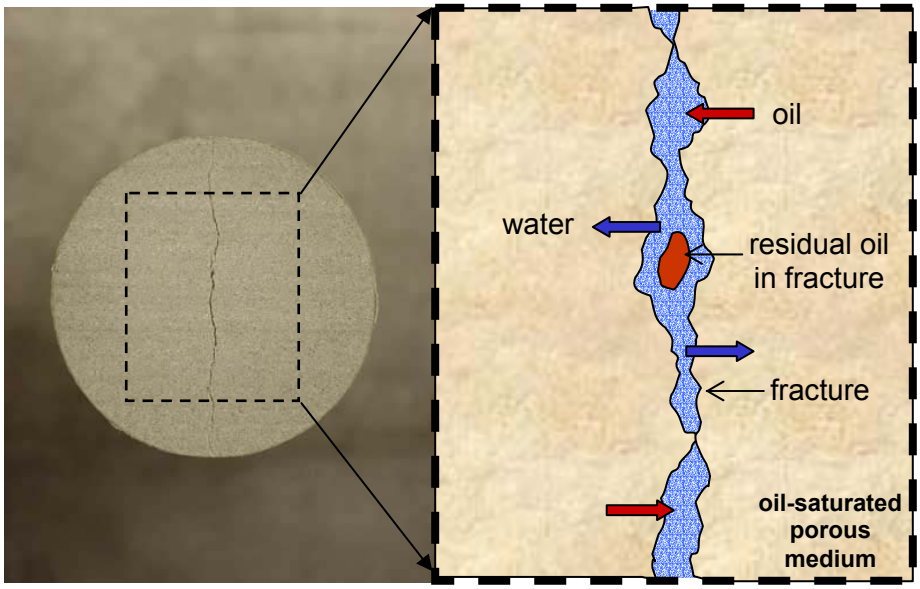

Figure 10: Schematic representation of capillary imbibition across fracture-matrix interface.

Capillary Imbibition across Fracture-Matrix Interface: In reservoirs with water drive, either from an aquifer or from water-flooding, the oil in the matrix adjoining a fracture is generally considered to be produced by water imbibition (Lee and Kang, 1999). In an attempt to study this mechanism, an imbibition experiment was conducted, allowing a wetting phase to enter the fracture and imbibe into the adjacent matrix. In addition to the experimental work, a series of simulation scenarios were performed to assist in understanding observations and the flow mechanisms taking place during capillary imbibition in fractured media. The experiment was performed in three stages: first injecting two small amount of water, and finally injecting water continuously. The sample used was a cylindrical Berea core, 47.5 mm long and 25.4 mm in diameter with a single longitudinal fracture with open ends.

The first stage of the experiment, stage 1, consisted of monitoring imbibition of wetting phase (water) in a fractured rock originally saturated with non-wetting phase (Soi=1.0). The rock had a single fracture in it, which extended along the full sample height. Water was injected upwards into the fracture for four minutes at a rate of 0.05cc/min, for a total volume injected approximately equal to the fracture void volume. The system was then closed and monitored using fast digital radiography (DR) and high-resolution CT scans. After several hours, when the imbibition process became too slow for changes to be appreciable, a second water injection took place (stage 2) and the system was again closed and monitored. In this second stage, a wetting phase imbibed into a sample containing both wetting and non-wetting phase (Soi<1.0). The third stage consisted of monitoring imbibition during continuous water injection. Fracture inlet and outlet were always open to flow during this stage. In the present document, only results from capillary imbibition 1 are described and analyzed.

Digital Radiography (DR) is an X-ray imaging technique with rapid digital processing that allows a much faster image collection than high-resolution CT scans do. However, speed is counterbalanced by limited image quality. DR was used in this experimental work to monitor the entire core during early-time saturation changes, which could not be accomplish using high resolution images. DR and CT scans also have a fundamental difference in the way images are collected. CT scans are used to visualize single slices through the object. A pile or stack of CT scans adjacent one another can therefore reproduce a three-dimensional digital view of the scanned object. DR reproduces not a slice but a full two-dimensional projection of the object exposed to X-rays. From DR images it is not possible to render a three-dimensional view of the scanned object. Figure 11 presents a DR of sample 2 at initial conditions, fully saturated with

the non-wetting phase. The color scheme in this figure represents the overlapped effect of the object's density and thickness. The vertical fracture is displayed in dark gray, meaning a reduced attenuation of X-rays penetrating the sample. Similarly, gray tones go from light to dark from the center outwards as the resistance is less due to the cylindrical shape of the core sample.

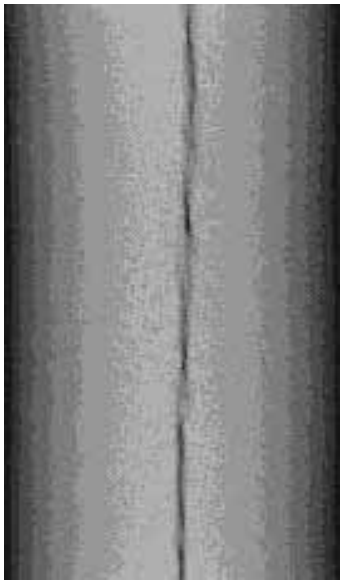

Figure 11: Digital Radiography of sample 2 initially saturated with oil.

To enhance the definition of the water front during matrix imbibition, the initial oil saturated DR image was subtracted from the DR images collected during the imbibition period. The outcome of this subtraction, presented in Figure 12, is a series of cumulative water saturation maps during capillary imbibition where water saturation increases with brightness. The nature of these images is merely qualitative; no saturation values have been assigned the DR's since they represent a lumped registration of a three-dimensional image.

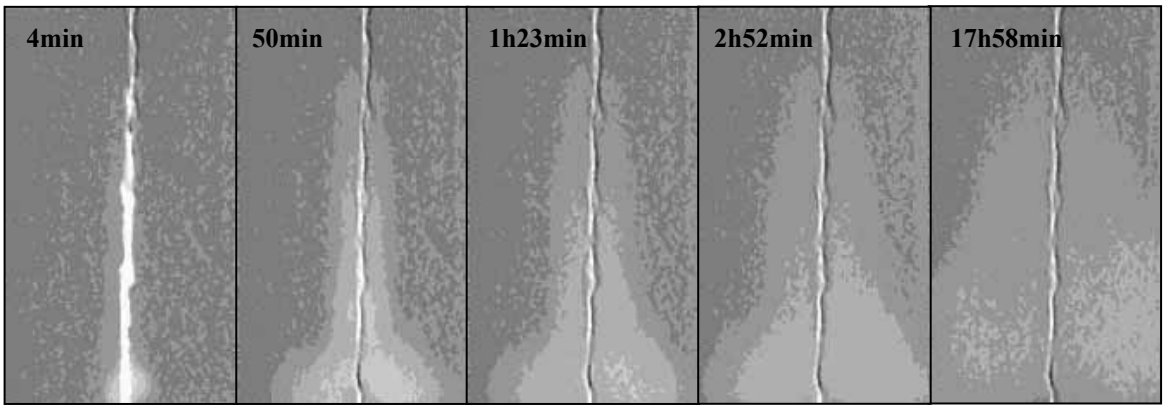

Figure 12: Cumulative water saturation during capillary imbibition obtained from digital radiography.

After four minutes of water injection (0.05cc/min) the system was closed and water continued to imbibe into the matrix under counter-current flow; oil is simultaneously migrating in the opposite direction (towards the fracture). When injection ceased, the fracture and its immediate adjacent matrix undergoes drainage.

The inlet face of the core was covered with Teflon, leaving a narrow gap for fluid to enter directly into the fracture. Nevertheless, it was quite difficult to fully isolate the face of the core from the injection channels in the flow distributor so that there was still some contact between the rock matrix and water in the inlet flow distributor. That is the main reason for a significantly wider saturation front in the lower portion of the DR (Figure 12). The bell-shape saturation front is especially visible at 50 minutes of monitoring time. The extent of water penetration into the matrix from the fracture is influenced by gravitational effects holding water in the lower portion of the core and also by the amount of water being exposed to the fracture-matrix interface at a given time. During upward injection, the lower section of the core is exposed to more water than the upper section at any given time. If matrix capillary forces are high enough to pull water from

the fracture before it reaches the top, then a wider water saturation front develops at the bottom of the core.

Images presented in Figure 13 were also obtained from the capillary imbibition experiment. These images represent the incremental changes in the water saturation profile between successive scans. The first image, e.g., is the result of the 0-minute image subtracted from one obtained after 4 minutes, the second image is the result of the 4-minute image subtracted from one obtained after 50 minutes, for a total of 46 minutes, etc.

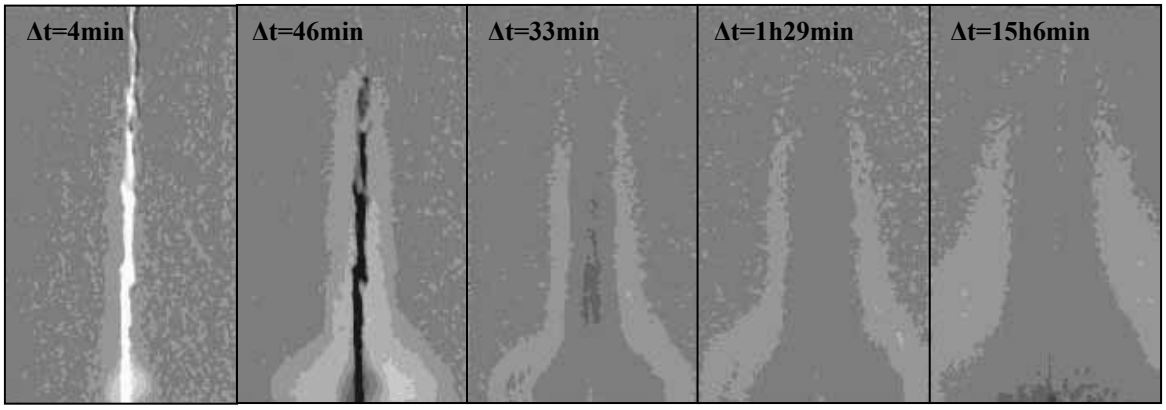

Figure 13: Incremental water saturation during capillary imbibition obtained from digital radiography.

The change in water saturation increases with brightness. Light gray represents regions where water has arrived (imbibition), dark gray represents regions from which water has been pulled (drainage), and middle gray regions experienced little change in saturation for the labeled time period. For instance, the 4-minute time frame image shows a very bright fracture indicating the arrival of water filling this space. In the next image (Δt=46 min), water saturation decreased in the fracture, while increasing in the adjacent rock. Water invasion grows not only in the

horizontal direction, but there also exists a vertical component that pulls the water upwards. The last frame in Figure 6.27 shows a significant advance in the vertical direction with water flowing from the center bottom of the core.

Image subtraction was also applied to high-resolution CT scans taken 3 mm above the bottom of the core. Results are shown in Figures 14 and Figure 15.

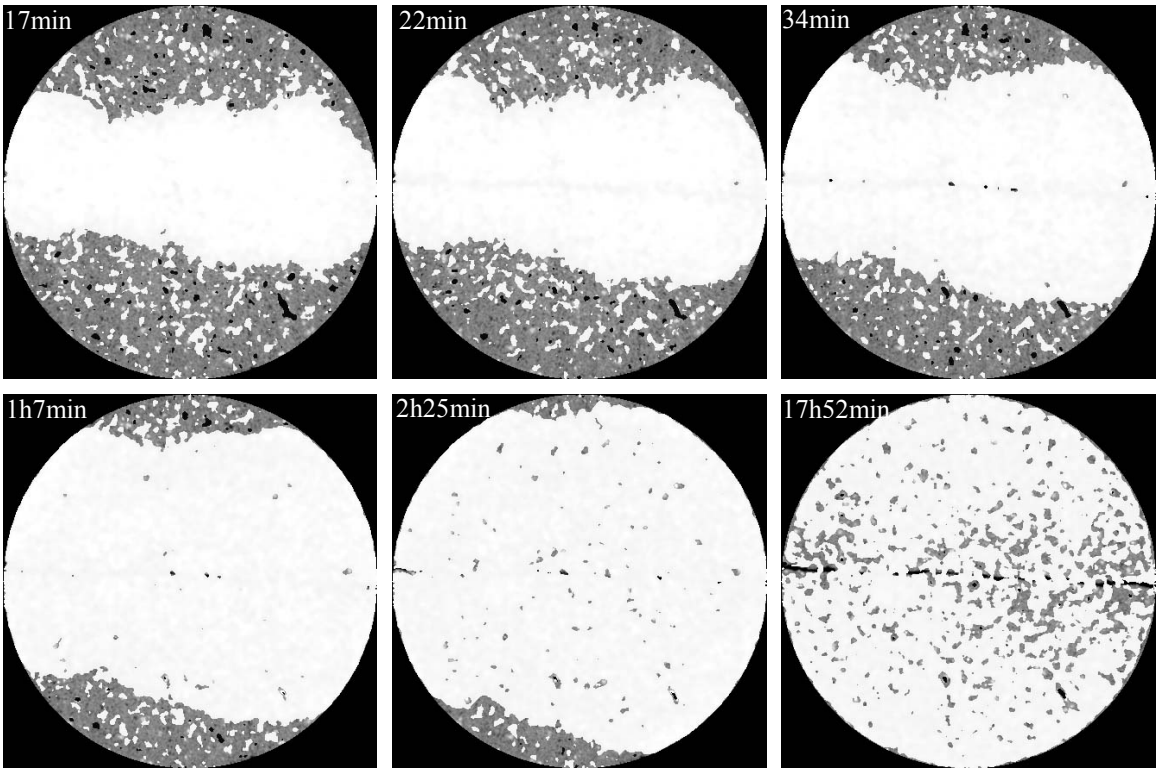

Figure 14: Cumulative water saturation during capillary imbibition obtained from high-resolution CT scans.

Figure 6.14 presents a series of cumulative water saturation maps where water invaded zones are denoted in white without consideration of saturation. The remaining areas in gray represent the original rock structure without water. Cumulative CT scans in Figure 6.14 show an uneven growth of the invading water front, which is mainly due to rock heterogeneities and boundary

effects. The rock sample used in this experiment (Sample 2) was cored parallel to bedding and fractured perpendicular to bedding. Thus the wavy water front is mostly caused by the contrast between the different layers in the matrix. The last image, corresponding to 17 hours and 52 minutes of spontaneous imbibition, shows sparse spots with a reduction in water saturation with respect to the previous image at 2 hours and 25 minutes. These spots are shown in gray and black, and remained after the complete water invasion, suggesting that water is transported in the direction perpendicular to the CT scanning plane. Recall that DR's also showed a significant water advance in the vertical direction, perpendicular to the CT scanning plane, with water flowing from the center bottom of the core.

Figure 15 shows the incremental changes in water saturation during spontaneous imbibition. White represents imbibed regions, black represents drained regions, and the remaining gray areas show the original rock structure where no significant change in saturation has taken place for a given time period. The first image in this sequence, at 17 minutes, is the same for both cumulative and incremental saturation distributions. The effect of rock layering on the development of the imbibing front is dominant during early time imbibition. Black spikes perpendicular to the fracture clearly follow rock layering patterns in the 5-minute frame in Figure 6.15. These spikes tend to correspond to layers with low density, which are characteristic of high porosity/permeability. The presence of these black spikes indicates that drainage is preferential to high porosity/permeability layers after they were initially invaded by water.

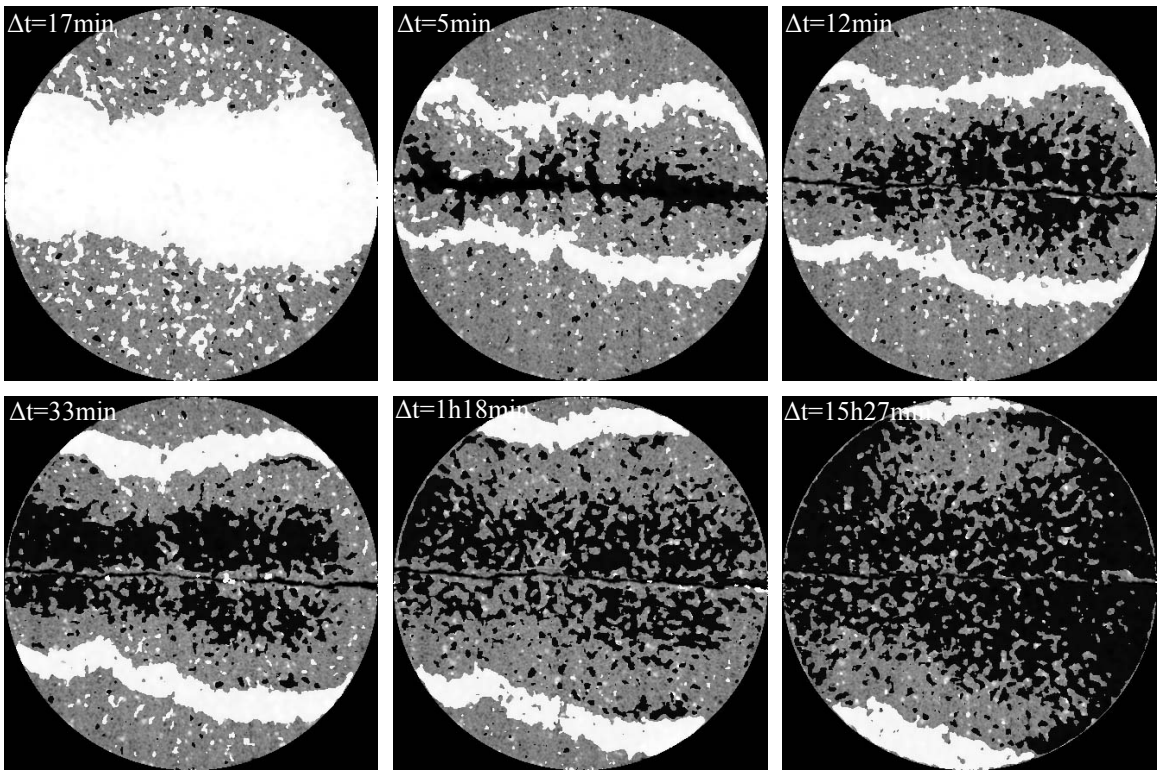

Figure 6.15: Incremental water saturation during capillary imbibition obtained from high-resolution CT scans.

Bedding planes in the matrix determine the shape of the imbibing front. Figure 16 shows a close-up of the 5-minute frame highlighting three layers, and a schematic drawing of those layers. The distribution of imbibed and drained regions in this figure provides evidence of the in-situ flow mechanism. The white water front reaches farther in low permeability layers and it is retarded in high permeability layers. Simultaneously, high permeability layers exhibit a larger drained area in black, which indicates that they supply water to the advancing water front. The imbibing front advances farther through low permeability layers due to higher capillary forces, while cross-layer fluid exchange tends to level the imbibing front.

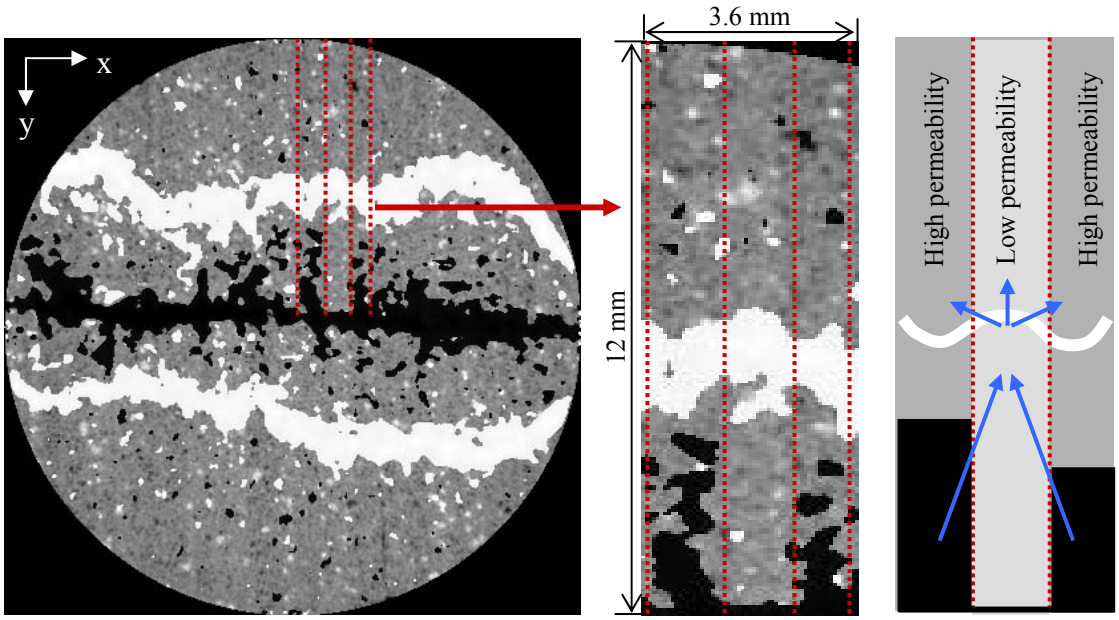

Figure 6.16: Effect of rock bedding on spontaneous imbibition from subtracted CT scans.

Low porosity/permeability layers in the rock tend to coincide with the narrowest fracture gaps where water is predominantly available, thus promoting advance of the imbibing front through those low permeability layers. The gray transition zone between the black and white contours in Figure 16-left indicates that no significant saturation change occurred during this time period. This transition zone is a major contributor to fluid transport, but its overall saturation shows little-to-no changes.

Saturation profiles were computed over a rectangular portion of the CT slices and averaged in the "x" direction. A schematic representation of this procedure in presented in Figure 17. The resulting profiles capture saturation changes with time in the direction perpendicular to the fracture and parallel to rock layering.

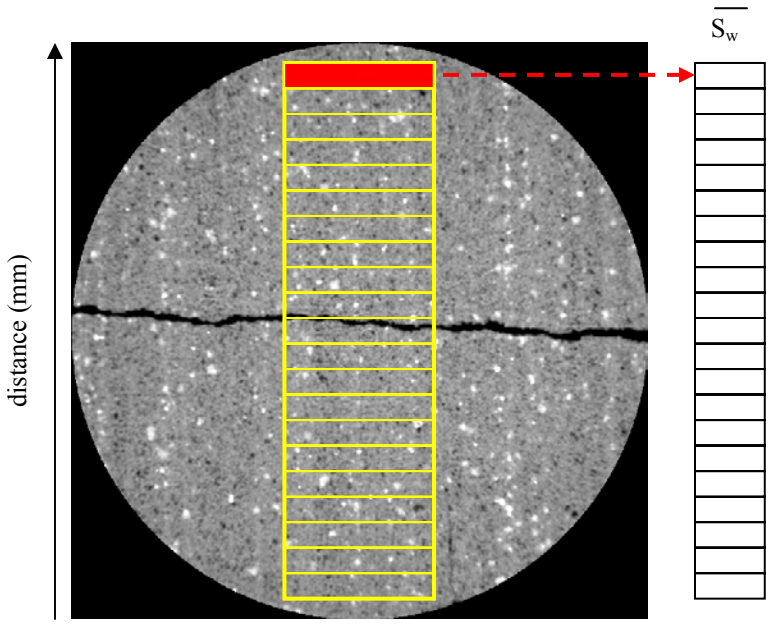

Figure 17: Schematic representation of the CT section used for saturation profile calculation.

The profiles obtained are shown in Figures 18 and 19 for cumulative and incremental imbibition fronts. Each of the six profiles in Figures 18 and 29 corresponds to a different time equivalent to those presented in Figures 14 and 15.

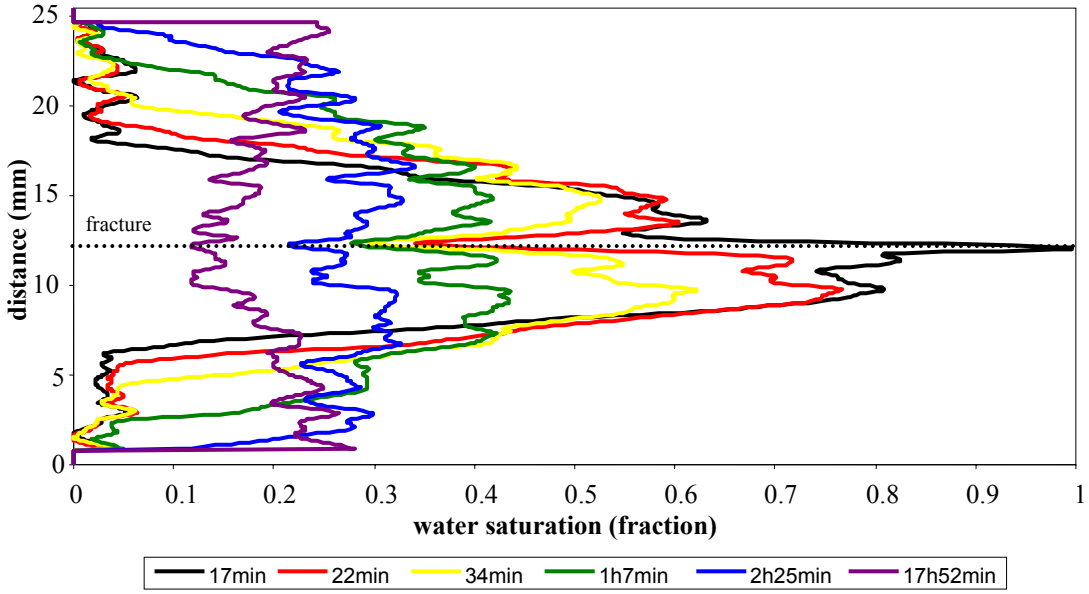

Figure 18: Cumulative water saturation profiles obtained from high-resolution CT scans. Horizontal orientation 3 mm above the inlet end of the sample.

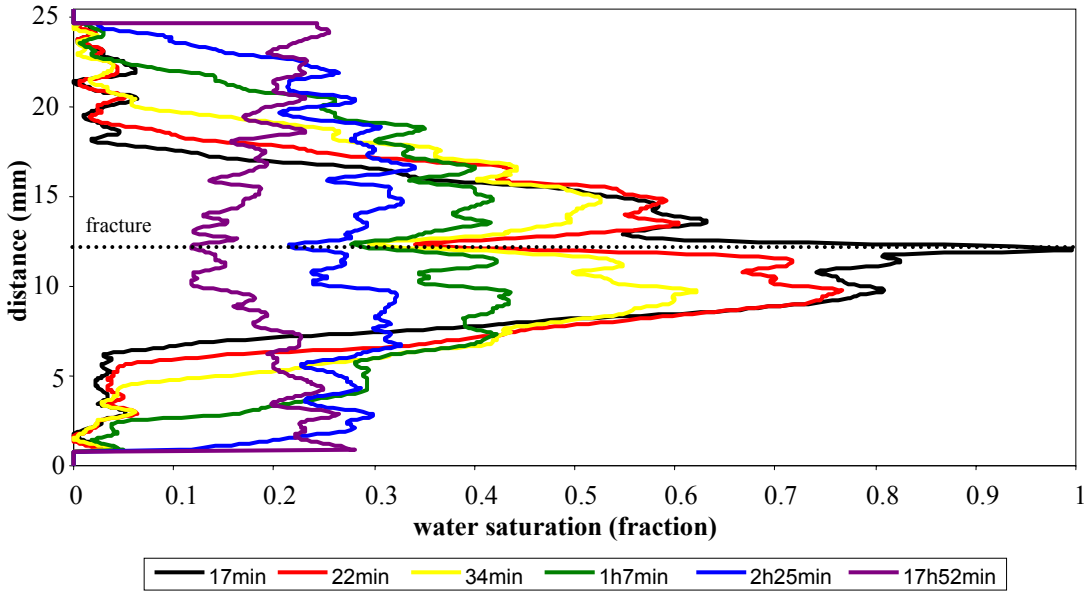

Figure 19: Incremental water saturation profiles obtained from high-resolution CT scans. Horizontal orientation 3 mm above the inlet end of the sample.

The first profile in Figures 18 and 19 (black), obtained after 17 minutes of spontaneous imbibition, shows a high peak of water saturation around 12 mm, which corresponds to the location of the fracture. This saturation peak is an indication of the channeling of water through the fracture gap. Five minutes later, at 22 minutes of cumulative imbibition, water resident in the fractured rapidly flows into the matrix. This mechanism is represented in the saturation profiles by a shift between the black and red lines near the fracture (12 mm). The red peak is inverted with respect to the black profile for a sharp reduction in water saturation in the fracture. As time progresses, the profiles tend to flatten with water spreading away from the fracture.

Average water saturations for each time profile in Figure 18 were calculated and plotted as a function of time. Results are presented in Figure 20. During early-time imbibition the average water saturation on the scanned slice is close to a constant 0.25, which suggests that fluid exchange takes place on the scanned horizontal plane. This observation and the symmetry of the imbibing front with respect to the fracture are strong evidence of the prevailing counter-current flow of oil and water near the fracture-matrix interface. However, after 100 minutes of spontaneous imbibition, Figure 20 shows a decrease in average water saturation, which indicates that water in migrating out of the scanning plane, in the direction perpendicular to the CT plane. Thus there must be a balance between early-time counter-current flow near the fracture-matrix interface and longitudinal flow component.

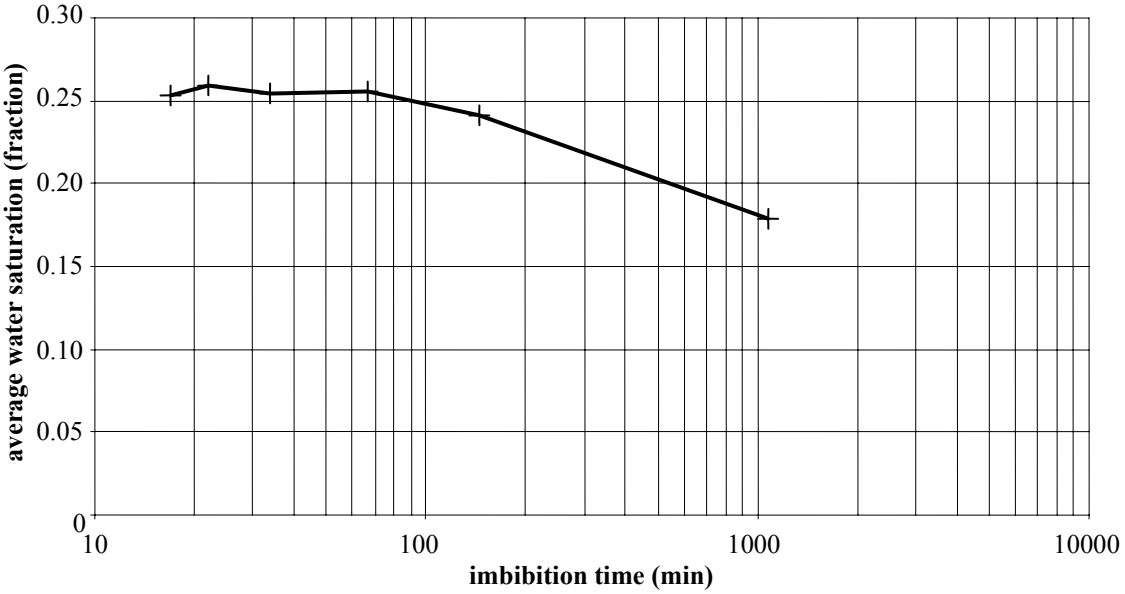

Figure 20: Changes in average water saturation as a function of time for a CT slice 3 mm above the bottom of the core.

An additional indication of counter-current flow perpendicular to the fracture plane is the presence of saturation banks in the rock matrix. Similar saturation banks have been observed in previous counter-current flow experiments using unconsolidated sands (Briggs and Katz, 1966 and Karpyn, 2001). The presence of saturation banks during two-phase flow in consolidated sandstones has not been previously reported in the literature. Figure 21 shows a three-dimensional portion of lower end of the fractured sample that was scanned after 18 hours of spontaneous imbibition. In this figure, a saturation bank is represented by the blue-green halo with low water saturation that is adjacent to the fracture and surrounds pockets of high water saturation (orange-red).

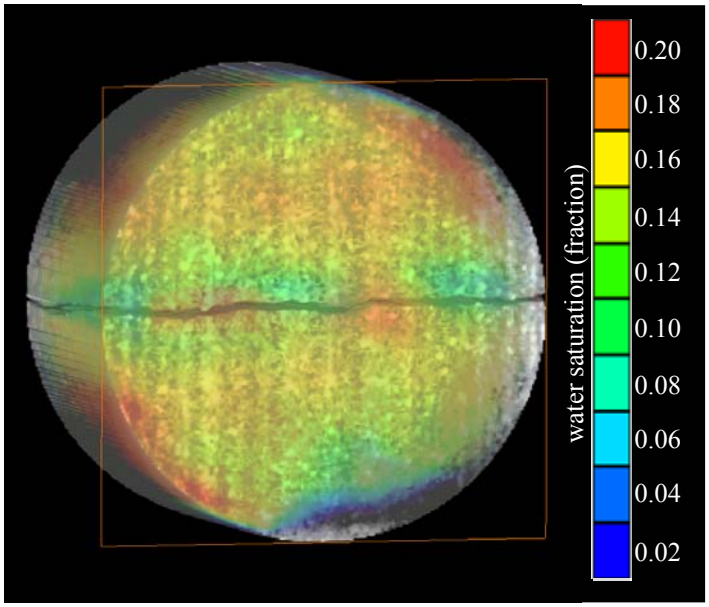

Figure 21: Water saturation map at the end of capillary imbibition 1 showing fluid banks, 1 mm above the bottom of the core.

Figure 22 also shows a blue halo around the fracture, indicating low water saturation. Low water saturation adjacent to the fracture surface could also be explained by the presence of micro fractures developed during the fracturing process. Micro fractures adjacent to the fracture-matrix interface may be responsible for an increase in local permeability. Previous observations demonstrated that water flows from high permeability layers, which is consistent with the saturation map in Figure 22.

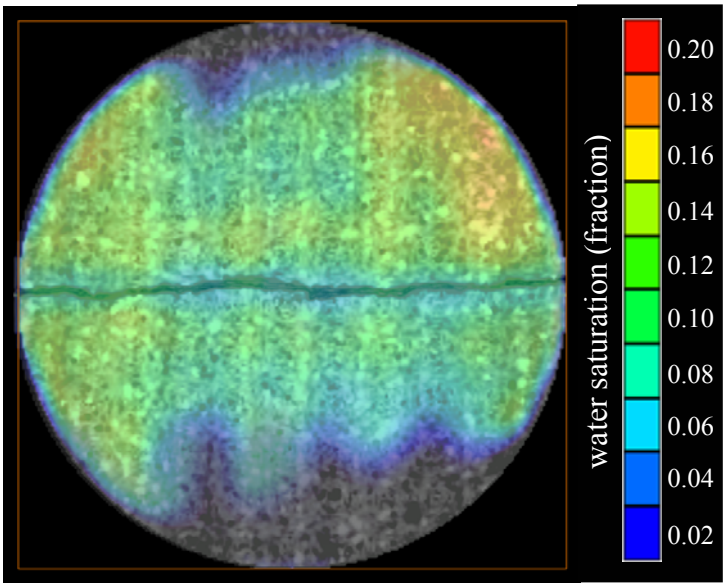

Figure 22: Water saturation map at the end of capillary imbibition 1 showing fluid banks and layering effect, 9 mm above the bottom of the core.

In summary, non-destructive monitoring of fluid flow in fractured samples allowed visualization of localized co-current and counter-current flow during capillary imbibition. Counter-current flow prevails in the direction perpendicular to the fracture surface, while co-current flow dominates longitudinal imbibition, parallel to the fracture plane. The presence of bedding planes in the rock's structure determines the shape of the imbibing front. The imbibing front advances faster through low porosity/permeability layers due to higher capillary forces, and cross-layer fluid exchange tends to level the imbibing front. These experimental observations are schematically represented in Figure 23. Additional confirmation of these observations was found through numerical simulation of capillary imbibition using a commercial reservoir

simulation tool. The next stage of the research is to perform conceptual modeling of the experiment in order to understand the fluid flow mechanisms that are taking place.

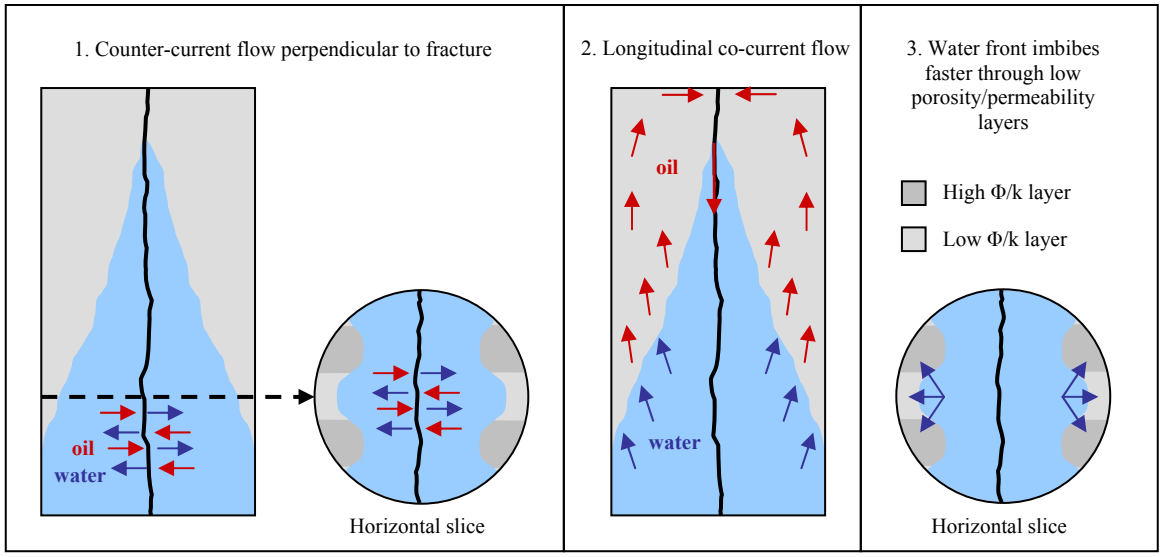

Figure 23: Schematic representation of experimental observations during capillary imbibition.

SHEAR FRACTURES – PERPENDICULAR TO BEDDING

Introduction

Fractured reservoirs are highly heterogeneous and usually provide significant challenges to appraisal and development teams. Fractures in reservoirs have a great impact on fluid flow patterns and on transport mechanisms. The study of two-phase flow transport in fractured porous media is important in a variety of engineering fields. In petroleum engineering, multi-phase fluid flow in fractured rocks is essential for maintaining and enhancing oil and gas recovery. Natural and artificially induced fractures are channels through which fluids can flow towards a production well. Fractures also have a significant impact in subsurface contaminant transport. In cases where two-phase displacements are dominant, the presence of a fracture network may cause fluid bypassing, early breakthroughs, reductions of sweep efficiencies, and overall decreases in productivities.

Fractures may also be non-conductive and form barriers to flow. An understanding of displacement processes in the presence of fractures can improve recoveries from oil and gas reservoirs. The two types of fractures found in reservoirs are shear fractures and extensional fractures. Shear fractures occur when the shear forces caused by anisotropic stresses are greater than the frictional strength of the rock. It results in the formation of a damaged zone, also known as gouge, parallel to the fracture. Due to the formation of the gouge, the relationship between conductivity and the shear fracture geometry is more complicated than for tensile fractures. The effect of two-phase flow is particularly important for petroleum engineers to understand the migration of oil/water in to the reservoir or to understand the flow path during recovery

processes. The lack of literature on the impact of induced shear fracture on two-phase flow is the motivation behind this work.

Many researchers have studied the effects of normal stresses on fluid flow or fluid-matrix interactions, concentrating on the variable apertures and asperity geometry of the fractures,{Iwai et al., 1976}, {Raven and Gale, 1985}, {Alajmi and Grader, 2000}. The vast majority of these studies have not focused on shear fractures because of complexities involved in analyzing the shear fracture due to the gouge formation.

Very few researchers have concentrated on the impact of shear displacement on the permeability or aperture of the fracture. These are all single-phase tests performed with flow either parallel or perpendicular to the shear direction or radial from the centre of specimen. In Makurat, et al., 1985, the author used a biaxial cell to investigate the effects of shear displacements on hydraulic conductivity and provided experimental data.

Based on the results from these laboratory experiments, the major factors controlling the permeability of single fractures and fracture cross-flow are the stress dependent fracture aperture, tortuosity, the fracture surface properties like roughness, fracture wall strength, the fracture normal stress, shear displacement related dilation and gouge formation. He concluded that whether fracture conductivity and fracture cross-flow increase or decrease with ongoing shear depends mainly on these parameters and the stresses acting in the fracture plane. Teufel (1987) presented the results of an experimental study of shear loading on the permeability and orientation of the fracture with respect to the flow. The results indicated that the permeability

decreased with increasing shear deformation due to the gouge formation and localized deformation of the rock matrix along the fractures. The internal damage within the gouge, which involved cataclasis and reduction in grain size and porosity, lead to the compaction of the gouge and therefore reduced the permeability in the fracture. Engelder (1974) and Jamison and Teufel (1979) showed that gouge is formed during shear deformation due to the cataclasis of grains along the sliding surface.

Esaki, et al., (1999) developed a coupled shear flow testing apparatus to study the effect of joint dilatancy and shear deformation on hydraulic conductivity. Since the fluid flow was in radial direction, the effect of shearing on the hydraulic behavior of the linear flow was not fully understood. The hydraulic conductivity, kh, was calculated using the model suggested by Barton et al., (1985), and excluded the effects of gouge on flow path and conductivity. Gentier et al., (1997) studied the effects of shear direction and the injection flow rate on the directional anisotropy of flow for a given normal stress and showed that the recovery pattern evolved with the shear direction and shear phases.

An essential factor in controlling the permeability of fractures is aperture geometry. In Gentier e et al., (2000), the author provided a powerful tool for linking fracture geometry to the mechanical behavior of fractures under shear stress using laboratory experiments, images of fracture surfaces and reconstruction of fracture topography from surface profiles. Analysis of images of damage zones on fracture surfaces after shearing suggested that there is little damage during the first two phases of shearing, prior to the peak shear stress. Damage is initiated in areas of the fracture with the steepest slopes. Yeo et al., (1998) studied the different characteristics of fracture aperture and

channeling flow, but could not exactly measure the aperture changes during compression and shear loading.

There are no reported works on the effect of two-phase flow in shear-fractured porous media. The saturation in the gouge and the two-phase transmissivity along or across the fracture has not been studied. Fluid-flow in shear deformation is not clearly understood due to the large number of variable parameters involved, such as shear direction and extent of shear deformation, fluid-flow direction, dilatancy, injection and confining pressure, aperture geometry, etc. Unlike extensional fractures, the shear fracture aperture geometry cannot be easily determined due to the gouge formation and the rapid reduction in grain size and a higher degree of compaction of the gouge per increment of shear displacement.

Problem Definition and Approach

Description: During recovery processes from reservoirs, we have to deal with multiple fluid phases and fracture-matrix interactions. To ensure maximum recovery, it is essential to understand and predict multi-phase fluid flow processes in fractured porous media. Due to the formation of gouge, the relationship between conductivity and the shear fracture geometry is complicated. Also, there are no reported works on the effect of two-phase flow in shear-fractured porous media. The goal was to investigate two-phase flow patterns and saturations in a shear-fractured Berea Sandstone using x-ray computed tomography.

Approach: A shear fracture was induced sub-perpendicular to the bedding planes using a sophisticated bi-axial cell. An experiment was set-up to acquire two-phase flow data in shear fractured porous media. The morphology of the rock matrix and the shear fracture were characterized using computed tomography [CT]. The relationship between the shear fracture geometry and oil/water conductivity in the presence of residual oil or water saturation was determined by a combination of external measurements of fluid volumes, pressure gradients and internal saturation using micro-tomography. Saturation and porosity profiles of the fracture and the matrix were generated by the manipulation of the acquired CT data.

The experimental set-up consisted of oil/water interactions through the rock sample in a pressurized core holder. A confining pressure of 500 psig was used on the cylindrical Berea sandstone sample to emulate the reservoir conditions. Sodium iodide (5% by wt) and Kerosene were used to represent water and oil respectively. The experimental procedure was divided in to various stages. Initially, the tracer is injected in to the potassium chloride saturated sample to determine the preferential flow path and to observe the fluid front. In the second stage, the sample is saturated with the kerosene until irreducible water saturation is achieved. This stage gave an insight in to the migration process that had resulted in the oil displacing the water over thousands of years. In the third stage, the sample was flooded until irreducible oil saturation was achieved. This helped us to understand the fluid flow during the recovery process when multiple fluid phases are introduced. During all these stages, X-Ray CT scans of the sample are taken and then manipulated to extract the required information. Our goal is to look in to the two-phase flow patterns and saturations of shear fractured Berea sandstone using x-ray computerized tomography.

The main objectives of this research are to qualify and quantify the effect of an artificially induced shear fracture on two-phase fluid flow. In this work, a shear fracture sub-perpendicular to the Berea bedding plane is studied. First, an experimental set-up is designed to analyze the multi-phase flow in shear fractured porous media. The morphology of the rock matrix and the shear fracture is then characterized using computed tomography (CT). The relationship between the shear fracture geometry and oil/water conductivity in the presence of residual oil or water saturation is determined by a combination of internal saturation and structure measurements using micro-tomography. Saturation and porosity profiles of the fracture and the matrix can be generated by the manipulation of the acquired CT data.

EXPERIMENT

The experimental procedure included core preparation and fracturing, permeability measurements, and two-phase flow experiments.

Core Preparation and Fracturing: A cylindrical Berea Sandstone cored sub-perpendicular to the bedding planes was used. The grains in the sample are fine and well sorted with closely placed planar bedding. The physical characteristics of the core are given in the table 2.

Table 2: Physical characteristics of the Berea Sandstone core

Length (cm)	Diameter (cm)	Porosity (%)	Weight Dry (gm)	Weight Wet (gm)
6.38	2.53	18	73.90	80.10

The porosity of the sample was measured by vacuum saturating the sample. The core was immersed in ethanol and placed on a stirrer to remove any fine particles clogging the pores. It was then dried overnight in an oven at 50 degrees C. The sample was jacketed in heat shrinkable teflon to keep the gouge and the matrix intact after fracturing. Figure 24 shows the cylindrical, teflon jacketed core used in the experiments. The induced shear fracture is clearly visible in Figure 25.The thin line running the whole length of the sample, lighter in color in comparison with the matrix, is the damage zone.

Figure 24: Berea sandstone core after fracturing.

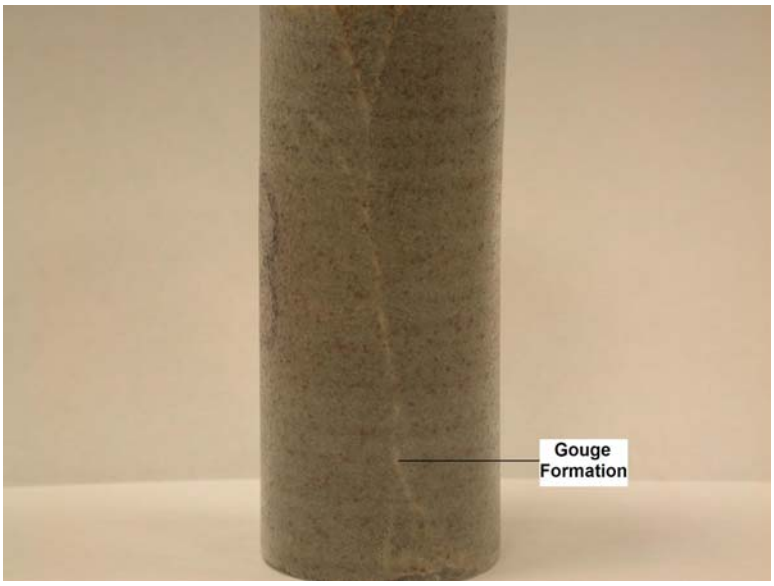

Figure 25: Berea sandstone core after fracturing.

In Pepper et al., (1954), the author states that Berea Sandstone, also known as Berea grit, is Mississippian terrestrial sandstone. Outcrops of Berea Sandstone in Ohio are found infilling previously cut channels in the underlying red Bedford and Chagrin shales. He also states that the lower unit, referred to as the Orange Berea, is coarser-grained and poorly sorted than the Upper Berea Sandstone unit, which is more frequently used in core flood experiments. In Churchel et al., (1991), the author states that Berea consists of 80-90 % quartz and about 3-6 % of feldspar, cemented by quartz, dolomite, clays and traces of iron sulphides.

The core was fractured in shear mode under a constant strain rate and a fixed radial confining stress. The fracturing of the sample was performed in a sophisticated bi-axial loading apparatus, Figure 26 with servo controlled loop, at room temperature and humidity. The Hook cell containing the rock sample, shown in Figure 27 is subjected to simultaneous compression and axi-symmetric confining pressure. The confinement effect, that is, the strengthening of the rock by the application of confining pressure p, is realized only if the rock is enclosed in an

impervious jacket. The confining medium used was hydraulic oil. An axial load of 450 pound-force was applied to the sample prior to the application of confining stress of 2925 pound-force. This was done to reduce or eliminate the occurrence of tensile fractures. The experiment was run at a displacement of 3 micrometer per second. The shear fracture was induced under water-saturated conditions. After failure, the sample was displaced by 0.5 mm and the total displacement was 1125 microns.

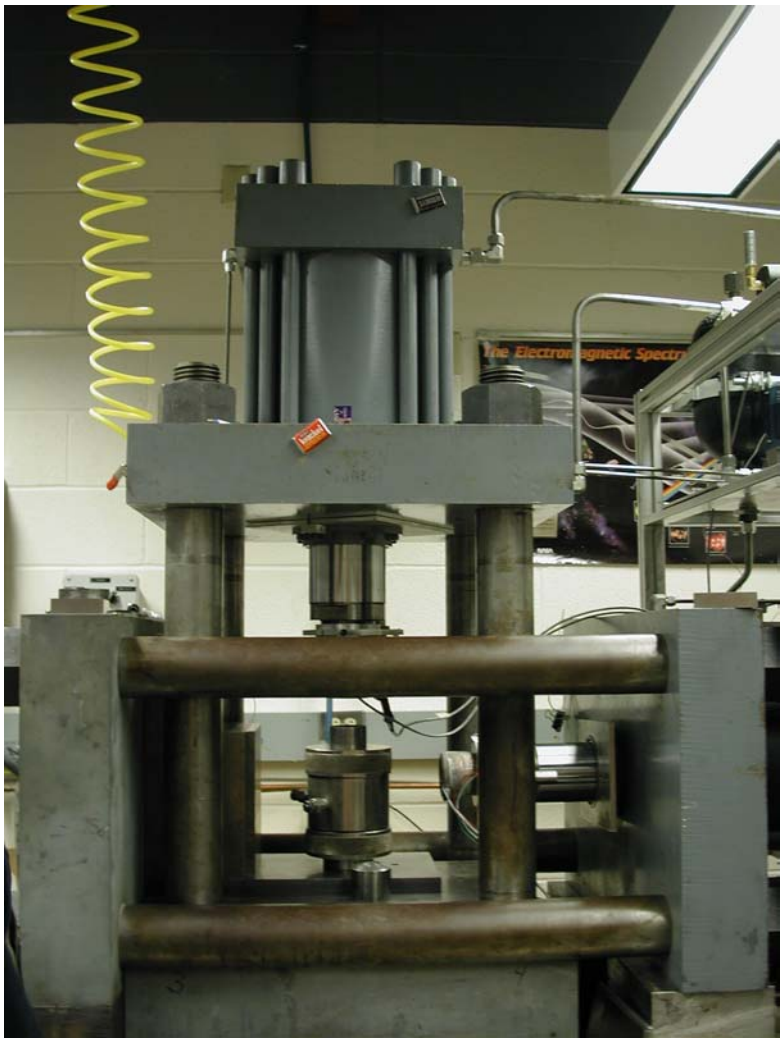

Figure 26: Shear fracture system setup.

Figure 27: Packing the sample with aluminum oxide beads in the Hoek cell.

Permeability Measurements: The permeability experiments were conducted before and after the fracturing of the sample. The procedure is detailed below:

a. The core was packed in the Hook cell and put under a confining pressure of 500 psig, to seal the rubber jacket which held the core and to simulate the reservoir conditions.

b. Vacuum was applied on the sample from the top of the core holder to evacuate the core prior to the injection of the fluid. The vacuum system consisted of a vacuum trap, a vacuum gauge and a vacuum pump.

c. 3% by weight of KCl-tagged water was introduced at the bottom of the core holder and flowed until the sample was completely saturated. A vacuum level of approximately 90 microns

of mercury was reached prior to the introduction of brine. Potassium chloride solution was used so as not to mobilize the clay particles.

d. KCl-tagged water was pumped at a rate of 0.1 cc/min for a period of 12 hrs, to ensure equal distribution of NaI-tagged water in the core. A 2-cylinder dual flow Quizix QL-700 pump was used for brine injection and metering.

e. Differential pressure data for several specific flow rates were collected. Differential pressure measurements are essential for determining absolute permeability. The pressure lines at the top and the bottom of the core-holder were connected to the paroscientific model 1020-D Digiquartz Intelligent Transmitter with an operating range of 0-20 PSI. The data logging was set for every 5 seconds and digitally recorded.

Two-Phase Flow Experiments: The flow experiments were conducted in three different stages. The experimental set-up consisted of the fluid saturation system, the core assembly, the pressure system and the CT x-ray scanner.

Two immiscible fluids, distilled water and kerosene were used to represent water and oil phases, respectively. The distilled water was tagged with 5% by weight sodium iodide to obtain a high CT signature. Kerosene has a low CT signature. The CT contrast between the water and the oil helps to visualize and analyze the displacement processes. Kerosene is a strong drying agent and therefore was kept in contact with distilled water to maintain equilibrium and to ensure that the kerosene does not dry out the sample.

The experiments followed these steps:

a. The fractured core, saturated with potassium chloride solution was placed in the core holder shown in Figure 28 The core holder, with an outer diameter of 2 inches, consists of an aluminum tube threaded at both ends with carbon fiber as outer covering for better resolution during the scan. Two stainless steel end plugs are fitted at each end. The core is centered by a teflon disc and placed in a rubber jacket that transmits the radial confining pressure of 500 psig. Both end plugs are provided with o-rings to seal and prevent the loss of fluids form the core holder. The two end plugs are held in place by two brass end caps, threaded at the exterior.

Figure 28: Core Holder

b. The entire sample was scanned using the high resolution x-ray CT scanner OMNI-X. The sample was scanned while potassium chloride solution was pumped in at a rate of 0.1 cc/min. The experimental set-up is shown in Figure 29.

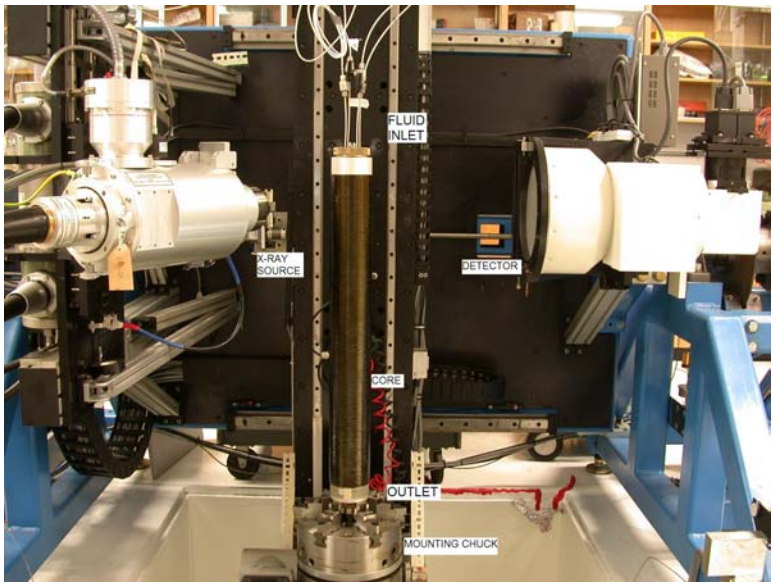

Figure 29: Experimental Setup: OMIN-X scanner and the core holder.

c. Water tagged with sodium iodide was injected into the sample at various stages. The core was scanned at various positions after injecting 0.5cc, 1.5cc, 4.5 cc. This was done to determine the fluid front and the flow paths. The NaI-tagged water injection continued overnight at a rate of 0.1 cc/min to ensure equal distribution of NaI in the core. The entire sample was scanned at the end of NaI-tagged water injection.

d. Kerosene was injected and the produced water was collected and quantified. The residual water in the core was about 46.5%. The entire sample was scanned at the end of kerosene injection.

e. NaI-tagged water was again injected into the core and the displaced oil was collected. The entire sample was scanned at the end of the water-flood.

A total of 1927 slices were collected at each stage through a core length of 6.39 cm. The slice thickness was 33.5 microns. A micro-focus x-ray source was used with tube voltage and current of 180 kV and 0.8 mA respectively. The in-plane pixel resolution was 25 microns. Each rotation consisted of 2400 views. A single rotation generated 41 slices and a total of 47 rotations were required to cover the entire length of the sample.

The fluids were injected from the top to overcome gravitational effects. A 0.5-micron filter was used to prevent the clogging of the flow distributor or the pore spaces in the rock sample. Pumpworks, Quizix's pump control software, was used for data logging and the operation of the pumps, QL-700 and SP-5200. All the operating data were recorded directly to the hard disk of the computer and were immediately available for review, analysis and graphing.

At the top of the core holder, total of 3 injection lines were used. The core holder was placed on the mounting chuck and oil and water were injected using two different lines. A bleeding line was used to change fluids. The injection flow lines converged at the flow distributor in the core holder. The injected fluids were collected at the bottom by the flow collector and sent out through the fluid outlet. The plastic tubing provided flexibility in the positioning and rotation of the core holder during CT operations.

Results and Analysis:

The topology of the fracture and the distribution of fluids in the sample were determined through several sequences of x-ray Computed Tomography (CT) scans at a voxel resolution of about 0.03 mm. To perform the data analyses, several computer programs were developed in PV-WAVE, preserving the spatial resolution provided by the scanner. The software package VoxelCalc, by Kehlco, and Amira were used to visualize and process the CT data.

Permeability: Absolute permeability quantitatively measures the ability of a porous medium to conduct fluid. Differential pressure data for several specific flow rates were collected. The permeability was determined by applying Darcy's law: $Q=(KA\Delta p)/\mu L$

, where Q is the flow rate, K is the permeability, A is the area of the sample, m is the viscosity, Δp is the differential pressure and L is the length of the sample.

Figure 30 shows the permeability calculations for the core, before and after the induction of the fracture. As can be seen from Equation (1) the slope of } $\Delta p/L$ vs. Q/A gives the permeability in Darcy.

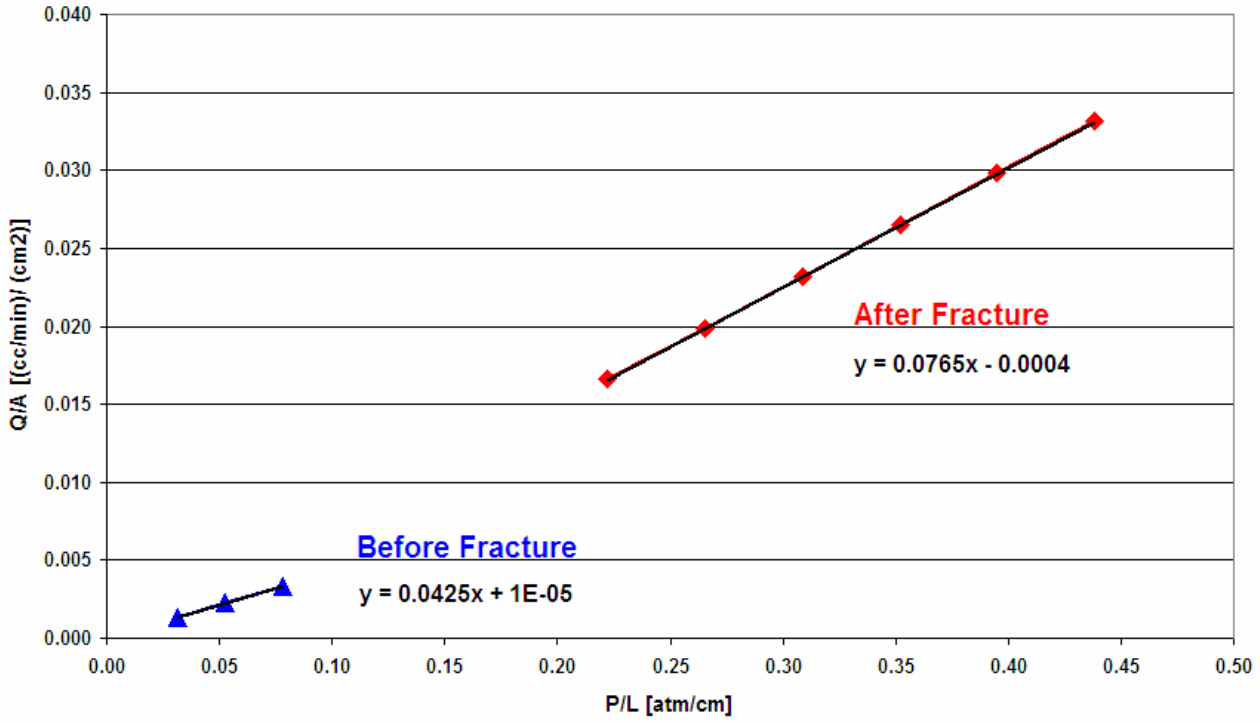

Figure 30: Plot of flow rate/area vs. pressure gradient.

The permeability before fracturing was 42.5 md, and has increased after fracturing to 76.5 md. The permeability has increased by 80% after the failure: shear displacement. This is a very large increase in permeability and implies significant flow through the fracture. The sample was displaced by 0.5 mm after fracturing and this may have resulted in the propagation of fine connected micro cracks in the fractured zone. Offset of the rugous fracture may also produce conductive fracture along the fracture plane.

CT Analysis: In addition to characterizing the fracture, x-ray CT data can be analyzed to map fluid saturation. As the x-ray passes through the object being scanned, the signal is attenuated by

scattering and absorption. The equation for the decay of intensity of an x-ray bean passing through a material is given by Beer's law: $I = I_o\, e(-\eta\chi\rho)$

, where Io is the initial x-ray intensity, η is the mass absorption coefficient (cm^2/g), x is the length of the x-ray path through the sample (cm) and ρ is the apparent density of the material (g/cc). Values of I/I_0 are converted to CT numbers by the computer software.

In this study, CT numbers range from 0 to 5000 for dense materials. The CT scale is arbitrary and is not an absolute representative of any property. The CT scanner was calibrated to a section of the core saturated with potassium chloride solution, and other conditions related to this base.

The first step of data analysis was to reconstruct the images at two different matrix sizes, 256 x 256 and 1024 x 1024. The CT values were then manipulated to reduce the noise in the acquired data. The images were then 'cut' to eliminate the rubber jacket and to change all the CT number values outside the core diameter to -1000. The 'cut' images were saved as 870 x 870 or 219 x 219 matrices, which reduces the computer storage space and manipulation time. The average CT number of a particular slice is then the arithmetic average of all points with a CT value greater than -1000.

Figures below show the image number 602 at 4 different stages. The low CT numbers appear dark and the high CT numbers appear light in the images. The bedding planes were shifted by translation along the fracture. Thus the layers on opposite sides of the fracture are different.

a. Figure 31 is at 100% saturation of KCl-tagged water.

b. Figure 32 is at 100% saturation of NaI-tagged water. The water was tagged with 5\% by weight sodium iodide and has a high CT signature and therefore appears brighter.

c. Figure 33 was acquired at irreducible water saturation. The image appears less bright than the image in Figure 32 due to the lower CT signature of kerosene.

d. Figure 34 shows the core at irreducible oil saturation after a water-flood. This image is brighter than the image shown in Figure 33 due to a displacement of oil by water. The intermediate injection stages showed that fluid front advanced at the same rate in the fracture and the layers on opposite sides of the fracture. Preferential flow in the fracture was not observed.

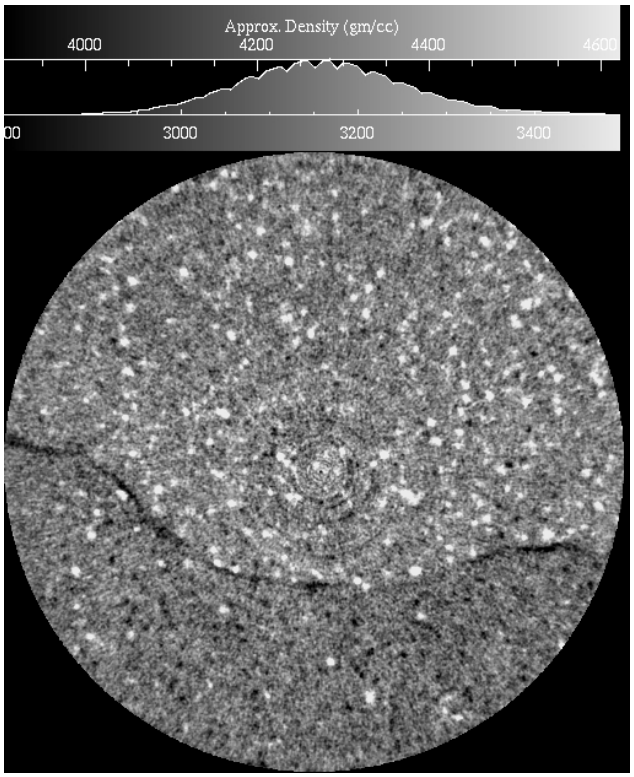

Figure 31: KCl-tagged water saturated core.

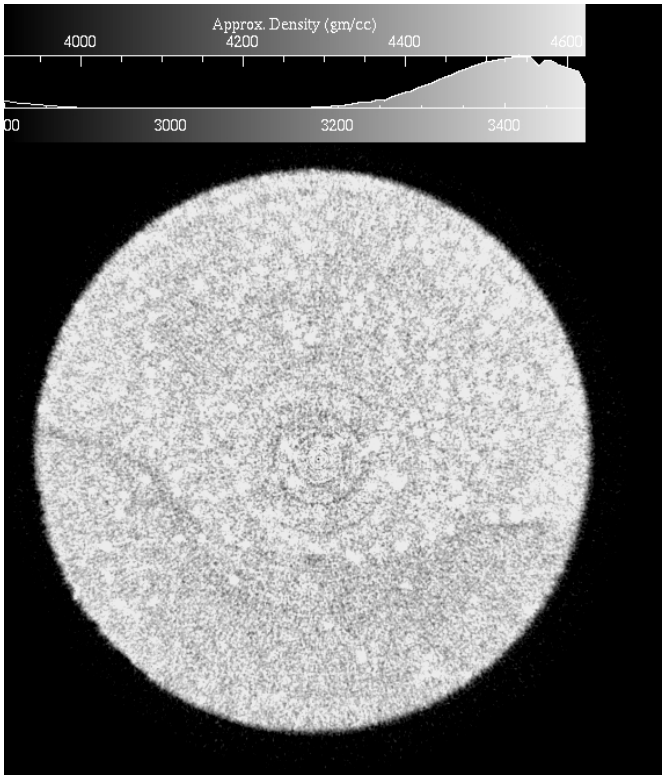

Figure 32: NaI-tagged water saturated core.

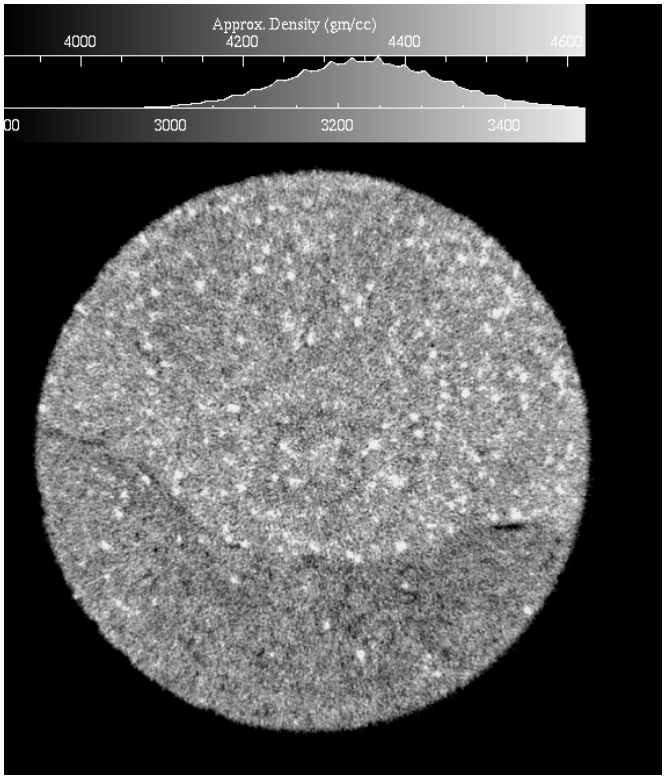

Figure 33: Core at residual water saturation.

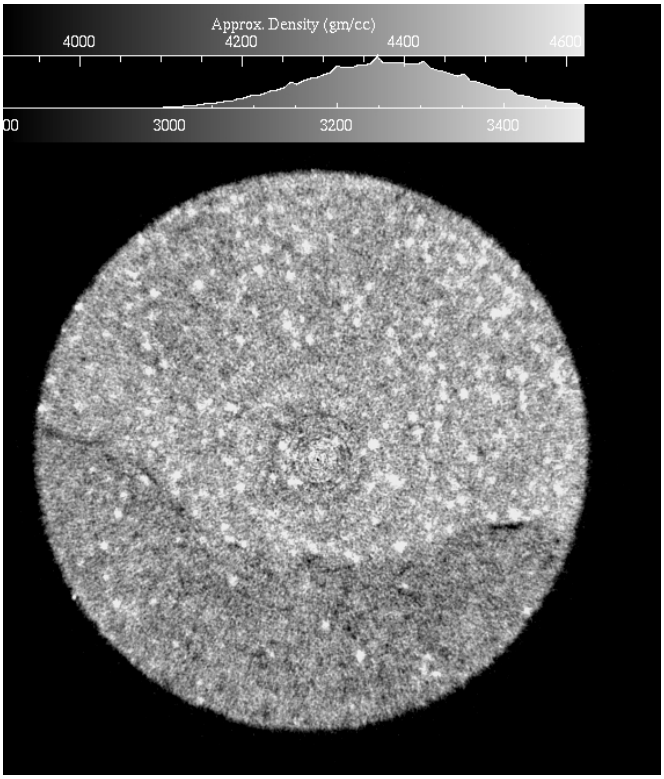

Figure 34: Core at residual oil saturation.

3-D Visualization:

A software package named Amira was used to visualize three-dimensional data sets. A state-of-the-art visualization and quantification technique helps to gain detailed insight into the data. The images were used to extract three-dimensional rendering and surface generation of the fracture itself from the rock matrix.

It was impossible to extract the fracture globally using a threshold CT value due to the significant differences in the CT values of the fracture in the high density and low density layers. The CT numbers of the fracture zone in the high density layers matched that of the CT numbers of the matrix in the low density layers. The damaged zone or the gouge formation formed near the fracture also contributed to the difficulty in identifying the fracture. Therefore, for a given

slice, the fracture was extracted manually by a combination of setting thresholds and testing connectivity of pixels. Extracted fracture data were used to create three-dimensional visuals of the fracture.

Figure 35 shows an a three-dimensional image of the fracture consisting of all voxels less than set threshold is highlighted in red and the layers of the sample are shown in a grayscale where high density material is in light gray. The fracture geometry is complex and does not lie along a straight plane from one end to the other. Much of this complexity is likely due to end effects where loading pistons contact the sample. The high density layers cutting across the fracture, which are light in shade and are perpendicular to the fracture, are also clearly visible in the figure.

The connected pores in the fracture can be seen in Figure 36. Here, only fracture voxels actually connected to each other are shown. The increase in the permeability after the fracturing can be attributed to the fact that the majority of the fracture voids are connected. The fracture was further characterized by identifying the major connected pores and calculating the volume of the fracture. Volume of the fracture was 75 mm^3, which is about 0.2% of the total sample volume.

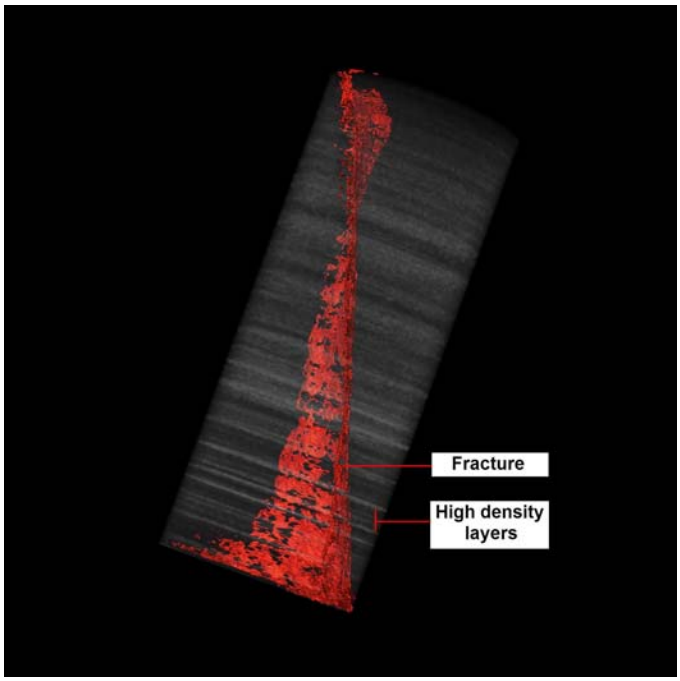

Figure 35: A three-dimensional rendition of the fracture.

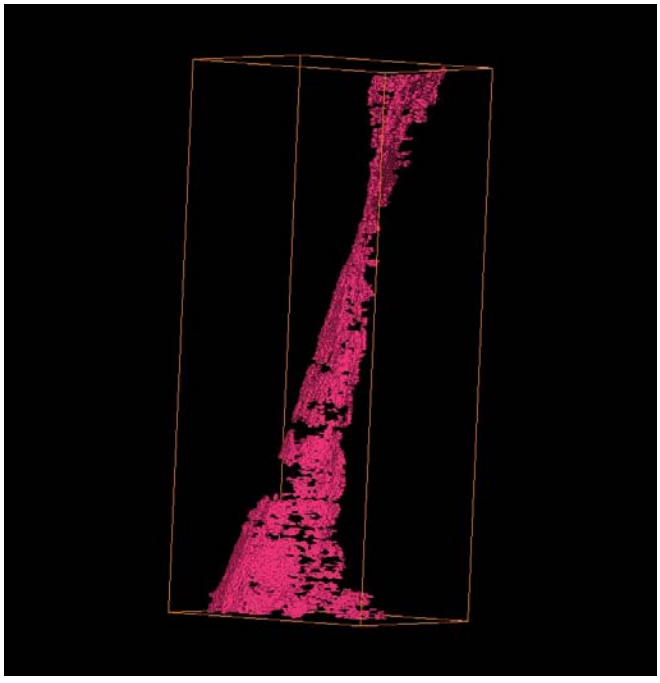

Figure 36: A three-dimensional rendition of the connected volume of the fracture.

Porosity: The overall porosity distribution in the core was obtained by following the procedure:

a. The KCl-tagged water saturated scans were subtracted from the NaI-tagged water saturated scans. The resulting images are the net CT values of tagged water in the core.

b. The change in the average CT values of the core were computed.

c. The average porosity was earlier measured to be around 18% from material balance. Change in the average CT values corresponds to the average porosity calculated and provided the basis for computing the porosity distribution. The voxel porosity was calculated as:

$$\phi_{voxel} = \phi_{ave} \frac{\Delta CT_{voxel}}{\Delta CT_{ave}}$$

d. The porosity of an individual voxel is proportional to the difference in CT numbers between the two data sets. The average porosity for every image was calculated from the voxel porosity distribution. The Figure 37 shows the average porosity in the sample. The average porosity for the images is 0.18.

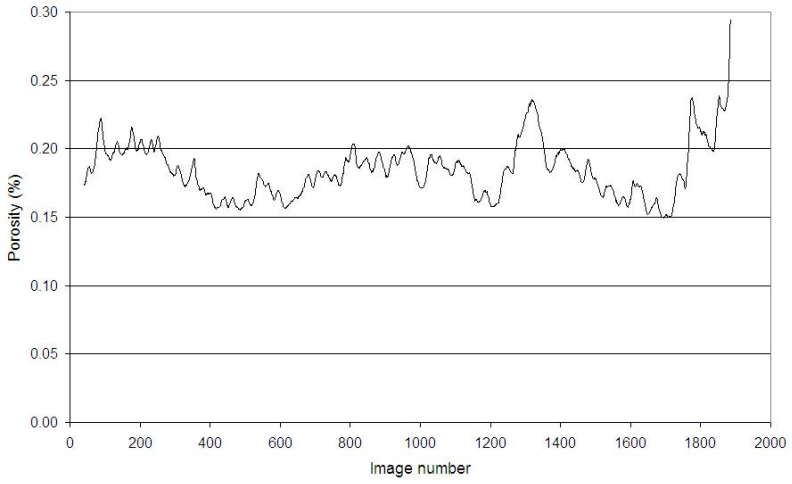

Figure 37: Average porosity along the entire sample.

Saturation mapping using CT data: near relationship was assumed between the average CT values for the core at 100 % brine saturation and at irreducible water saturation [S_{wirr} = 0.46] for the estimation of oil/water saturation in the core. The water saturation at each voxel was calculated using the linear interpolation equation as shown below:

$$s_{w,voxel} = 1 - \Delta CT_{voxel} \frac{0.54}{\Delta CT_{ave}} \frac{\phi_{ve}}{\varphi_{voxel}}$$

The value 0.54 is 1 – S_{wirr} and was experimentally determined. Applying the above Equation, the water saturations at irreducible water and oil saturations were calculated for the entire sample. The average was calculated and plotted for every slice and is shown in the Figure 38.

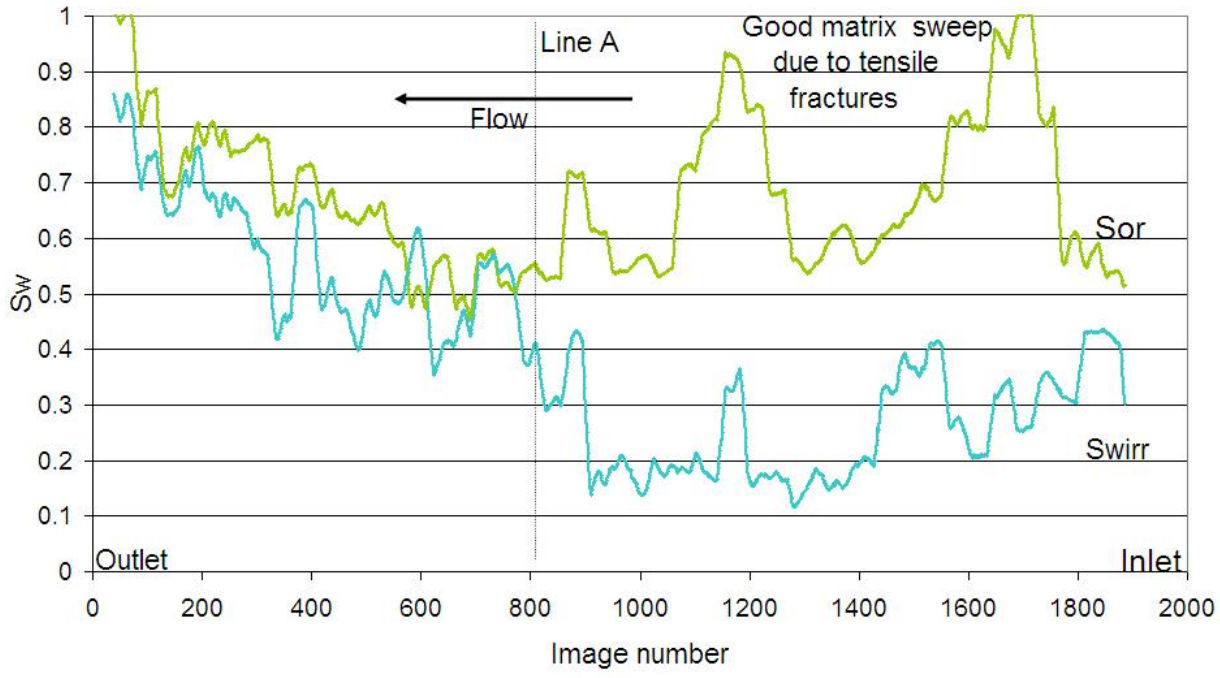

Figure 38: Water saturation and residual water condition and residual oil condition.

Figure 38 suggests that the two halves of the core sample behave differently. The two distinct regions are separated by the line A. The fluid inlet and outlet are marked on the graph.

The residual water saturation is higher in images 0-900 [the outlet side] compared to images 900-1927 [the inlet end of the core]. This suggests that the oil displaced more water at the inlet and as a result, the CT signature is low. The water saturation in the outlet section remains high as implied by the high CT signature. This pattern shows that the fracture is closed at the inlet section, forcing oil flow out into the matrix. However, oil displaces more water out of the inlet section. In the outlet section, the fracture is more open and acts as a conduit which results in poor matrix sweep.

The water saturation at residual oil conditions (after the water flood) is higher than the water saturation at S_{wirr}, as expected. The jumps in saturation of images 1420-1600 and 1600-1705 are due to the presence of high permeability layers and horizontal fractures. The water saturations for S_{or} and Swirr at the outlet section are comparable due to little or no matrix contribution to the fluid flow. As a result of fluid bypassing through the fracture, the sweep efficiency is low for both Sor and S_{wirr}. Figure 39 shows the difference in S_w between S_{wirr} and S_{or} vs. image number. The fracture is more open towards the outlet end of the core, leading to bypassing. At the inlet end, the fracture does not act as a conduit and forces the fluid to enter the matrix.

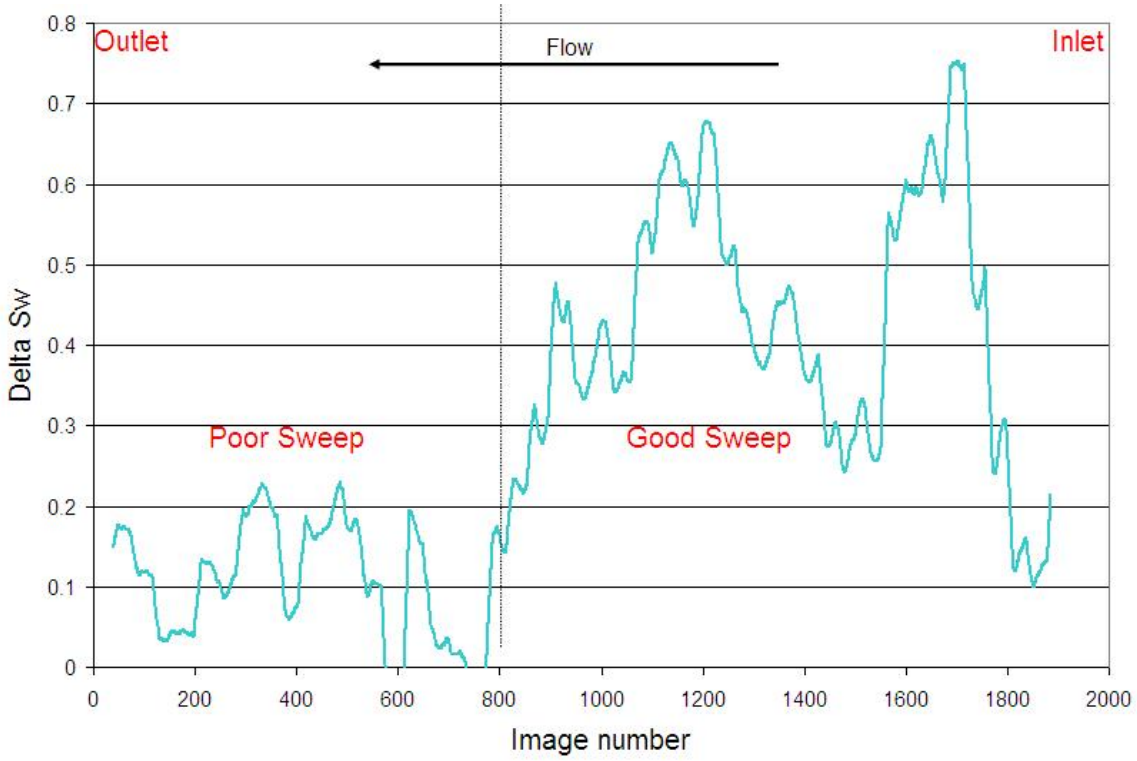

Figure 39: The difference in S_w between S_{wirr} and S_{or} vs. image number.

The average CT numbers of the slices are shown in Figure 40. At S_{wirr}, the CT values are low due to the low CT signature of kerosene. The CT numbers of the outlet section vary markedly from the inlet section. The CT numbers decreases as we move from the inlet to the center of the core and then increase towards the outlet. The CT values of the irreducible water saturation are comparable to the CT values at irreducible oil saturation at the outlet side of the sample [left half of the diagram]. Poor fracture permeability in the inlet section forces the oil into the matrix, leading to better sweep efficiency. At the outlet end, the fracture is more permeable and the oil flows in the fracture leading to poor matrix sweep. The same trend occurs at irreducible oil saturation at the end of the water-flood.

The above findings strongly suggest the role of the fracture as a channel at the outlet end and as a barrier at the inlet end. Figure 41 shows the connected pores in the fracture. At the inlet end, the fracture is not very continuous and has lots of asperities. The inlet end also indicates the presence of high density layers which disconnect the fracture. The fracture of the outlet end is continuous supporting our conclusion of channelized flow. There are no major breaks in the fracture at the outlet section.

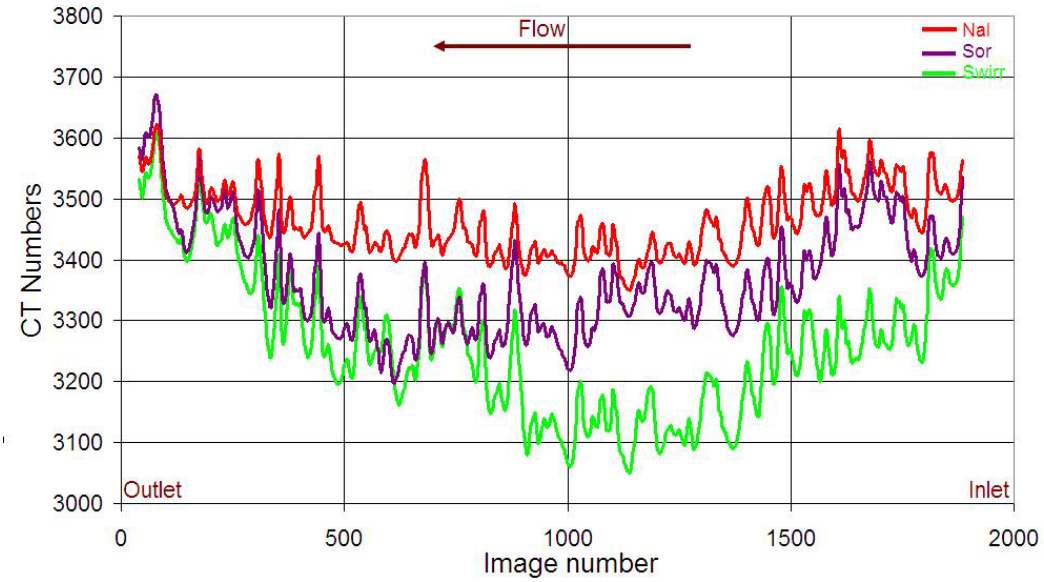

Figure 40: Average CT numbers per slice along the sample.

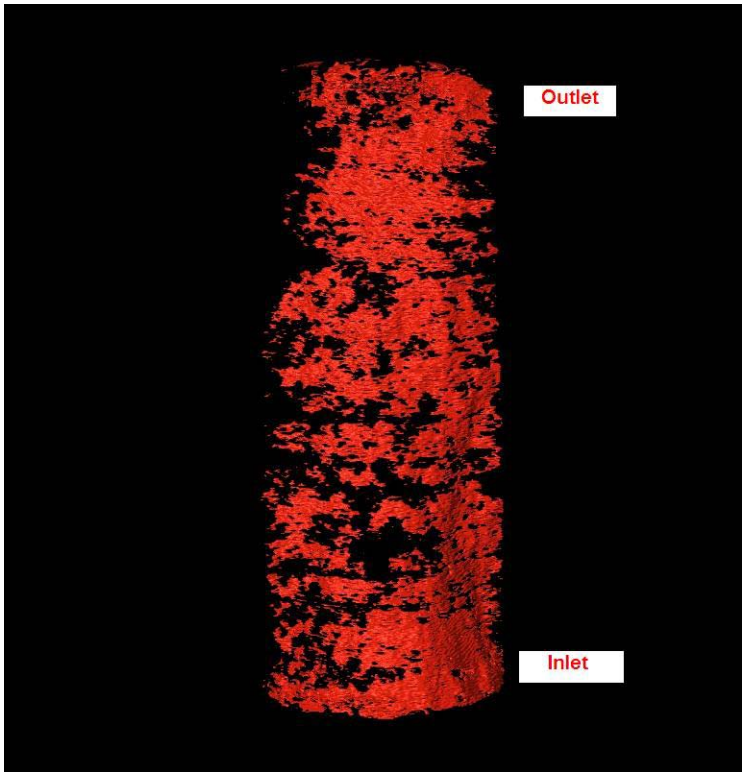

Figure 41: A three-dimensional rendition of the fracture. Black spaces indicate asperities.

Figure 42 shows a three-dimensional rendition of the entire sample. It is divided in to sections by individual planes, each tagged with scan numbers. The shear fracture is seen as the linear horizontal fracture. The shear displacement is clearly seen in the region between images 386 and 677, where the upper half of the sample was displaced to the left relative to the lower half of the sample. The following describes the nature of the different segment of the core shown in Figure 42.

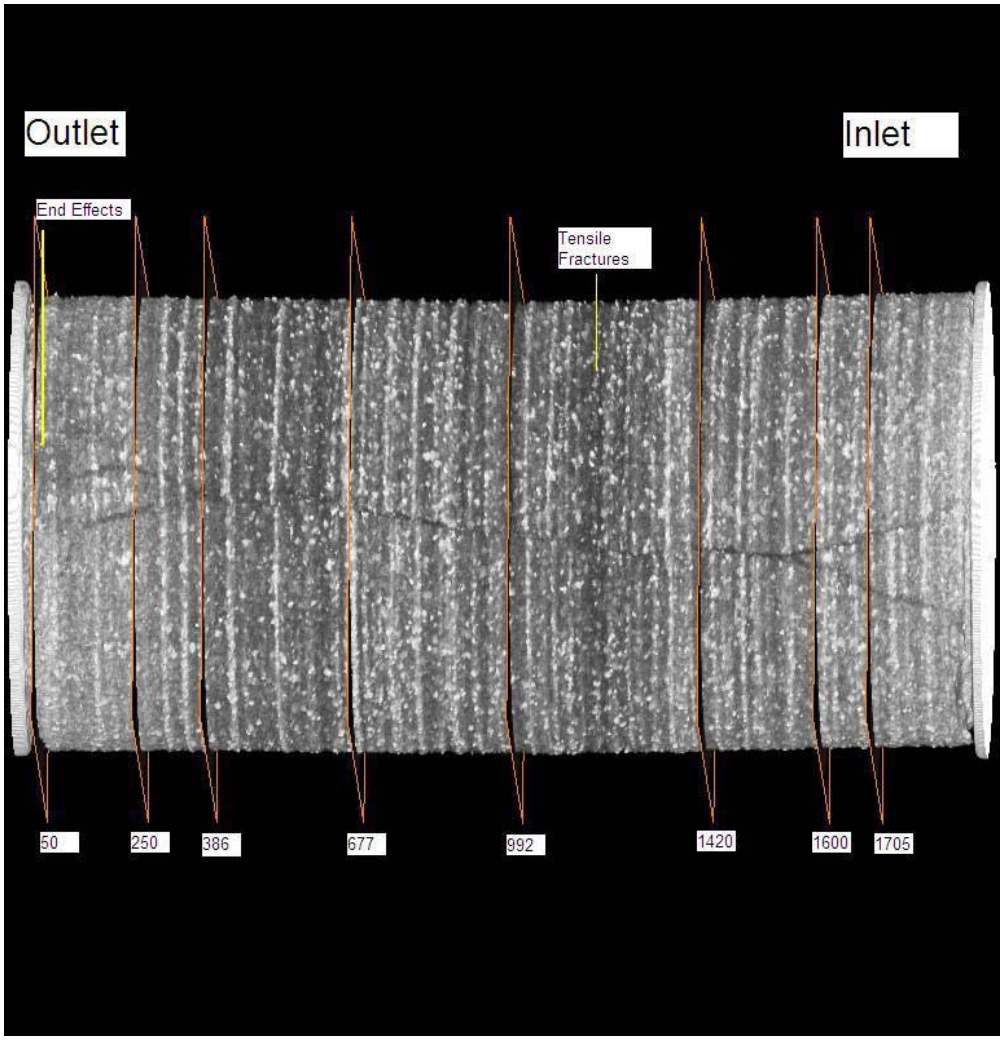

Figure 42: A three-dimensional rendition of the entire sample with the fracture on the surface.

a. Images 50-250: This section has multiple shear fractures along with horizontal fractures. The main fracture is open and causes low matrix sweep.

b. Images 386-677: The fracture is visible, which implies that the fracture is open. There is also a series of tensile fractures around image 600. Since the fracture is open, the fluids do not enter the matrix to a large extent. Due to the tensile fractures, the matrix sweep around image 600 is better when compared to images 0-300 [Figure 40

c. Images 677-992: This is the transition zone where two different behaviors can be noticed. The fracture is wide open from 677 to around 800 and suggests channelized flow. The numbers of high density layers are high, but it seems that the fracture has shifted the layers and created an opening. From 800-992, the fracture is not clearly visible due to the prominent damaged zone. There are a series of horizontal fractures around image 992, implying good matrix sweep.

d. Images 992-1420: The fracture is not pronounced and is only vaguely visible. Towards the middle of this section, there is a thick band of horizontal fractures which pushes the fluids into the matrix as the fracture acts like a barrier due to the thick damaged zone.

e. Images 1420-1600: The fracture is open and forks in to two branches. There are no horizontal fractures in this section and the flow in the fracture can be attributed to the relatively low difference between the CT numbers of S_{wirr} and S_{or}.

f. Images 1600-1705: The fracture is prominent in this section, but there are no horizontal fractures. This behavior of this section is similar to those of Images 992-1420

g. Images 1705-1927: The fracture is clearly visible. There are few horizontal fractures at the end due to the end effects. Shifting of the layers is not prominent. The fracture plays an

h. important role in the fluid transport, creating low displacement efficiency.

Figure 43 shows the fracture at one of the ends. It is clearly seen that the fracture is open at the outlet and therefore, the fluids can flow through it without sweeping much of the matrix.

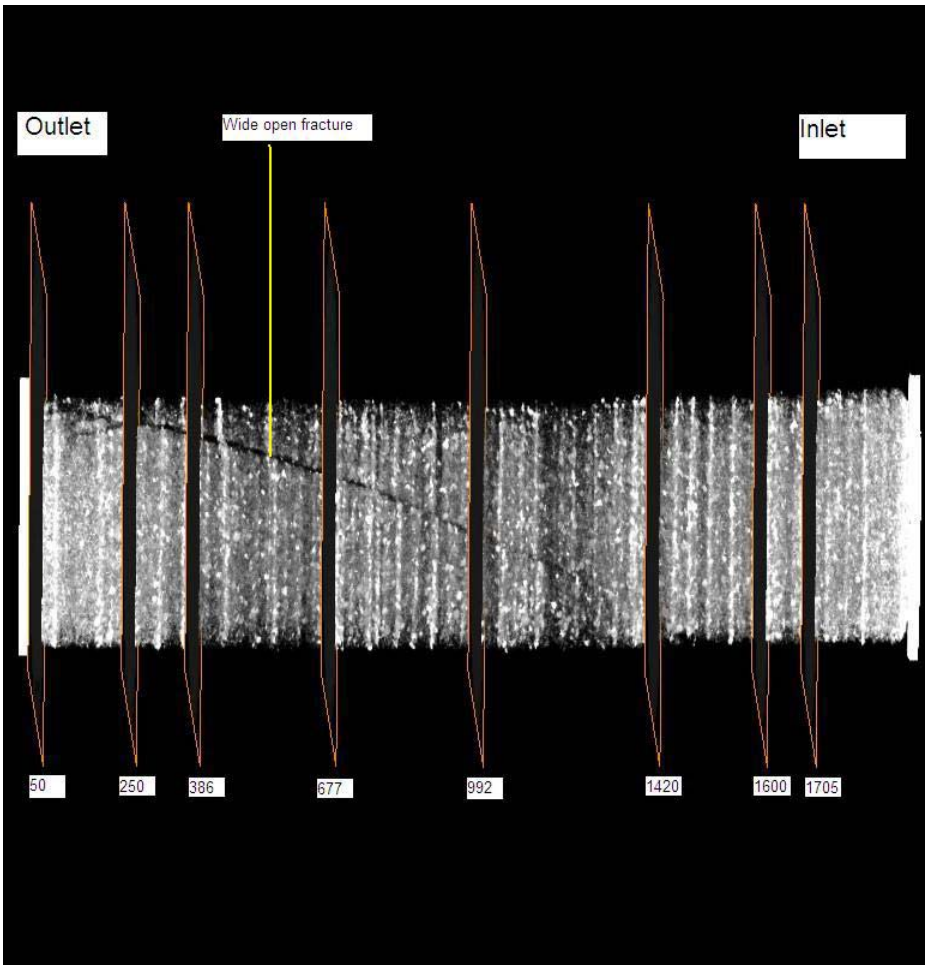

Figure 43: A two-dimensional axial slice through the core shown in Figure 42.

CONCLUSIONS

Summary: Presence of the induced shear fracture significantly increased the permeability [Table 2]. CT scans were used to look at the transport mechanisms in the fracture and the matrix. Poor fracture permeability at the inlet section forced the oil into the matrix and led to

better sweep efficiency. At the outlet end, the fracture acts as a conduit, leading to poor matrix sweep. The intermediate injection stages showed that fluid front advanced at the same rate in the fracture and the layers on opposite sides of the fracture. Preferential flow in the fracture was not observed.

Conclusions:

In single phase flow, an increase in absolute permeability does not imply an evenly distributed, permeable fracture. The open fracture can be towards one end of the core or distributed along the length of the core where the absolute permeability is infinite, thereby increasing the overall permeability significantly.

Regions where the fracture is non-conductive with a high number of horizontal fractures have good matrix sweep. Regions where the fracture is conductive have poor matrix sweep. In two-phase flow, the displacement of oil by water is more in high permeability layers compared to the low permeability layers.

The transmissivity across the fracture is not too different from that of the matrix as fluid fronts advanced at the same rate in the fracture and the layers on opposite sides of the fracture. Fluids from the matrix converge at the distributed open fracture throughout the core implying good transmissivity across the fracture.

REFERENCES

Alajmi, A. F., and A. S. Grader, Analysis of Fracture-Matrix Interactions using X-Ray CT, Proceedings of the SPE Eastern Regional Meeting, col123,
pp97-104, October 2000.

Barton, N., S. Bandis, and K. Bakhtar, Strength Deformation and Conductivity Coupling of Rock Joints, International Journal of Rock Mechanics and Mining Sciences & Geomechanics Abstracts, vol. 22, pp 121-140, June 1985.

Churchel, P. L., P. B. French, J. C. Shaw, and L. L. Schramm, Rock Properties of Berea Sandstone, Baker Dolomite and Indiana Limestone, Proceedings of the 1991 International Symposium on Oilfield Chemistry, vol. 68, pp 431-446,
February 1999.

Engelder, J. T., Cataclasis and the Generation of Fault Gouge, Geological Society of America Bulletin, vol. 85, pp 1515-1522, 1974.

Esaki, T., S. Du, Y. Mitani, K. Ikusada, and L. Jing, Development of shear flow test apparatus and determination of coupled properties for a single rock joint, International Journal of Rock Mechanics and Mining Sciences, vol. 36,
pp 641-650, 1999.

Gentier, S., J. Riss, G. Archambault, R. Flamand, D. Hopkins, Influence of fracture geometry on shear behaviour, International Journal of Rock Mechanics and Mining Sciences, vol. 37, pp 161-174, 2000.

Gentier, S., E. Lamontangne, G. Archambault, and J. Riss, Anisotropy of Flow in Fracture Undergoing Shear and its Relationship to the Direction of Shearing and Injection Pressure, International Journal of Rock Mechanics and Mining Sciences,vol 34, pp 412, 1997.

Iwai, k., Fundamental Studies of Fluid Flow Through a Single Fracture,
PhD thesis, University of California, Berkley, 1976,

Jamison,W. R., and L. W. Teufel, Pore Volume Changes Associated With Failure and Frictional Sliding of a Porous Sandstone, 20th US Symposium on Rock Mechanics, pp 167-170, June 1979.

Makurat, A., The Effect of Shear Displacement on the Permeability of Natural Rough Joints, Proceedings of the 17th International Congress of the International Association of Hydrogeologists, vol. 39, pp 99-106, 1985.

Pepper, J. F., Jr. W. Dewitt, and D. F. Demarest, Geology of Bedford Shale and Berea Sandstone in Appalachian Basin, United States Geological Survey - Professional Papers, vol. 259, pp 109, 1954.

Raven, K. G., and J. E. Gale, Water Flow in a Natural Rock Fracture as a function of Stress and Sample Size, International Journal of Rock Mechanics and Mining Sciences \& Geomechanics Abstratcs, vol. 22.4, pp 251-261, August 1985.

Teufel,, L. W., Permeability Changes During Shear Deformation of Fractured Rock, Proceedings of the 28th U.S. Symposium on Rock Mechanics, vol. 129, pp
473-480, 1987.

Yeo, I. W., M. H. De Freitas, and R. W. Zimmerman, Effect of Shear Displacement on the Aperture and Permeability of a Rock Fracture, International Journal of Rock Mechanics and Mining Sciences, vol. 35, pp 1051-1070, 1998

LIST OF ACRONYMS AND ABBREVIATIONS